CHRONOSTAR – II. Kinematic age and substructure of the Scorpius–Centaurus OB2 association

Maruša Žerjal [1,2,3,4]★ Michael J. Ireland [1] Timothy D. Crundall [5] Mark R. Krumholz [1,6] and Adam D. Rains [1]

[1]*Research School of Astronomy & Astrophysics, Australian National University, ACT 2611, Australia*
[2]*Centre for Astrophysics, University of Southern Queensland, Toowoomba, Queensland 4350, Australia*
[3]*Instituto de Astrofísica de Canarias, E-38205 La Laguna, Tenerife, Spain*
[4]*Universidad de La Laguna, Dpto. Astrofísica, E-38206 La Laguna, Tenerife, Spain*
[5]*I. Physikalisches Institut, Universität zu Köln, Zülpicher Str. 77, D-50937 Köln, Germany*
[6]*ARC Centre of Excellence for Astronomy in Three Dimensions (ASTRO-3D), Canberra ACT 2611, Australia*

ABSTRACT

The nearest region of massive star formation – the Scorpius–Centaurus OB2 association (Sco–Cen) – is a local laboratory ideally suited to the study of a wide range of astrophysical phenomena. Precision astrometry from the *Gaia* mission has expanded the census of this region by an order of magnitude. However, Sco–Cen's vastness and complex substructure make kinematic analysis of its traditional three regions, Upper Scorpius, Upper Centaurus-Lupus, and Lower Centaurus-Crux, challenging. Here, we use CHRONOSTAR, a Bayesian tool for kinematic age determination, to carry out a new kinematic decomposition of Sco–Cen using full six-dimensional kinematic data. Our model identifies eight kinematically distinct components consisting of 8185 stars distributed in dense and diffuse groups, each with an independently fit kinematic age; we verify that these kinematic estimates are consistent with isochronal ages for *K* dwarfs. Both Upper Centaurus-Lupus and Lower Centaurus-Crux are split into two parts. The kinematic age of the component that includes PDS 70, one of the most well-studied systems currently forming planets, is 15 ± 3 Myr.

Key words: stars: kinematics and dynamics – Galaxy: open clusters and associations: individual: Scorpius-Centaurus association – Galaxy: kinematics and dynamics.

1 INTRODUCTION

The closest site of a massive star formation to the Sun is Scorpius–Centaurus OB2 association (Sco–Cen), which spans a large area in the sky due to its proximity. The number of confirmed Sco–Cen members has grown over time, from just 512 stars in 1999 (de Zeeuw et al. 1999) to almost 15 000 candidate objects in 2019 (Damiani et al. 2019) thanks to the precision astrometry from the *Gaia* mission (Gaia Collaboration 2016a, 2018, 2021) that has enabled a more detailed view of the association. For example, Röser et al. (2018) report on a new dense subcomponent V 1062 Sco with ages of less than 10 to about 25 Myr at a distance of 175 pc.

Historically, Sco–Cen has been divided into three groups, namely Upper Scorpius (USCO), Upper Centaurus-Lupus (UCL), and Lower Centaurus-Crux (LCC), although Rizzuto, Ireland & Robertson (2011) argued that this split is arbitrary, especially for UCL and LCC. Wright & Mamajek (2018) suggest that Sco–Cen was likely born highly substructured, with multiple small-scale star formation events. As summarized by Preibisch & Mamajek (2008), there is evidence that star formation in the USCO was triggered by an event occurring in the adjacent but older UCL group. These three groups likely represent the remains of low-density, unbound star-forming

regions that began to disperse as soon as the star-forming gas was removed; such unbound regions account for ~ 90 per cent of all star formation in the Milky Way and similar galaxies (Krumholz, McKee & Bland-Hawthorn 2019), making them ideal testing grounds to study a wide variety of phenomena, from early stellar and planetary evolution, to the initial mass function, to the origin of the Galactic field population.

All of these studies, however, rely at least partly on reliable estimates of the age of the dispersing stellar population. Among the techniques available to provide such estimates, evolutionary tracks are the most frequently used approach for coeval ensembles of stars. However, model uncertainties, especially on the low-mass end, combined with unresolved binaries and intrinsic luminosity variability in young stars, often limits the precision of this method (e.g. Sullivan & Kraus 2021). On the other hand, kinematic ages based on the assumption that associations are gravitationally unbound and expanding provide a model-free alternative, albeit with a requirement for very precise measurements of parallaxes, proper motions, and radial velocities. There have been numerous attempts to estimate ages by tracing the orbits of stars back through time to the point when they were more concentrated than we observe today (e.g. LACEwING; Riedel et al. 2017), but even with the precision of *Gaia* astrometry, such efforts have generally yielded age estimates with very large uncertainties, and with poor consistency with alternative age-dating methods. The primary exception is Miret-Roig et al.

★ E-mail: marusa.zerjal@gmail.com

(2020)'s study of the Beta Pictoris association – their kinematic age of $18.5^{+2.0}_{-2.4}$ Myr compares well with the alternative techniques, for example Mamajek & Bell (2014)'s combined lithium depletion boundary and isochronal age of 23 ± 3 Myr.

Traceback efforts for Sco–Cen have thus far yielded conflicting results. Recently, Squicciarini et al. (2021) traced back the celestial coordinates of the Upper Scorpius members on the basis of their present-day proper motions and found 8 distinct kinematic subgroups divided into dense and diffuse populations. An analysis using *Gaia* DR1 data (Gaia Collaboration 2016b, ~400 stars) by Wright & Mamajek (2018) found no evidence that the three Sco–Cen subgroups were more compact in the past, but did confirm that the stars are gravitationally unbound and have a non-isotropic velocity dispersion. On the other hand, Bobylev & Baykova (2020) estimate a linear expansion coefficient of Sco–Cen to be 39 ± 2 km s^{-1} kpc^{-1}, based on T Tauri stars.

The lack of consistent results from traceback methods led Crundall et al. (2019, hereafter Paper I) to propose an alternative approach, implemented in the new code CHRONOSTAR, based on tracing proposed origin sites forward and comparing against the present-day stellar distribution; the principle advantage of trace-forward as compared to traceback is that it avoids the explosion of uncertainty that inevitably occurs when one attempts to trace backwards the orbits of stars whose position and velocity include observational uncertainties. In Paper I, we use CHRONOSTAR to obtain a kinematic age of 17.8 ± 1.2 Myr for the Beta Pictoris association in good agreement with the age estimate of Mamajek & Bell (2014). A further advantage of CHRONOSTAR's approach is that it simultaneously and self-consistently determines both kinematic ages and association memberships, rather than relying on predetermined membership lists (as is the case for traceback methods). This allows it to improve the extraction of the members, especially at the low-mass end where the spread in luminosity is large. Moreover, the lack of dependence on predefined membership lists allows CHRONOSTAR to discover new kinematic groups blindly, an ability that is particularly important for diffuse groupings whose overdensity might not be apparent in 2D or even 3D position space, but that become apparent in 6D phase space.

In this work, we upgrade CHRONOSTAR to enable efficient processing of larger data sets than in Paper I (Section 2) and use it to explore the kinematic substructure of the Scorpius–Centaurus association (Section 3). Section 4 addresses the individual components, while Section 5 validates their kinematic age. We present our conclusions in Section 6.

2 CHRONOSTAR

We first summarize the CHRONOSTAR[1] algorithm, referring readers to Paper I for a full description and a list of tests we have performed to validate the code. We then describe improvements made to the code since publication of Paper I, which we use here.

2.1 Summary of the CHRONOSTAR algorithm

CHRONOSTAR is a robust Bayesian method for kinematic age determination of young stellar associations. Its autonomous examination of the parameter space addresses the complex substructure of associations, their membership determination and evolution of the associated models. We model an association as consisting of one or more independent components, each of which is described by an

age and an initial (i.e. at age zero) distribution in the 6D Cartesian phase space XYZUVW. The spatial part of the coordinate system is centred at the Sun's projection on the Galactic plane, while the origin of the velocity is placed in the local standard of rest (LSR; Schönrich, Binney & Dehnen 2010).

For simplicity, the initial distribution of each component is approximated as an isotropic Gaussian, with the same standard deviation in all three spatial dimensions and all three velocity dimensions. In our model, time 0 corresponds to the time at which the stars transition from being gravitationally bound to moving on ballistic orbits through the Galaxy. In order to obtain the *present-day* distribution of stars in XYZUVW space, we trace each component *forward* in time to the present day. We compute the orbits using GALPY (Bovy 2015), with MWPotential2014 for the Galactic potential.

In order to fit the parameters describing each component (its kinematic age, origin point in 6D phase space, and initial dispersion in position and velocity), we compare the present-day distribution that results from the trace-forward to the observed distribution of members of that component in 6D phase space. In turn, we identify those observed stars that are most likely to be members of each component based on the overlap integral between the Gaussian describing the present-day distribution of that component and the Gaussian describing the error distribution of each prospective member star in 6D phase space, including the full covariances of the observational errors. The circular dependency – the need to know the members in order to fit the parameters describing each component, and the need to know the parameters of each component in order to determine which stars are members – is resolved using the Expectation-Maximization (EM) algorithm. This iterative algorithm starts from an initial guess of membership assignments, then fits the properties of each component for those assignments. Once the best-fitting component parameters have been found, the algorithm then fixes those parameters and recomputes the membership probabilities for each observed star. The algorithm then iterates until the parameters of each component and the membership assignments to them converge. The important advantage of this approach is that, because the membership lists are not fixed *a prori*, CHRONOSTAR can blindly discover new moving groups, study the substructure of known associations, and revise its membership census. This in turn enables the accurate determination of kinematic ages.

In addition to the EM step, CHRONOSTAR adds a third layer of iteration. The EM algorithm operates on a fixed number of components, but we do not know *a priori* how many components we should use to fit a given data set. To handle this problem, CHRONOSTAR starts assuming a single component, and after the EM algorithm converges, we split the resulting component into two components, then rerun the EM algorithm for those two components. We then compute the Bayesian information criterion (BIC), which represents the likelihood function penalized by the number of parameters in the model, for the one-component and two-component fits; if the BIC for one-component fit is preferred we stop, while if the two-component fit is preferred, we repeat the procedure, splitting the two components into three, and so forth, stopping once the BIC indicates that adding a further component may result in overfitting.

Since not all stars in the input catalogue are members of the association, we add another component that describes the field stars and name it a background component. The shape of the background probability–distribution function is estimated with a Gaussian Kernel Density Estimator (KDE) using 6376 803 *Gaia* DR2 stars with radial velocities and parallax errors better than 20 per cent. The overlaps with the background component are determined only once

[1] https://github.com/mikeireland/chronostar

at the beginning and held fixed through the fitting procedure. This component does not depend on any parameters and is held fixed, but otherwise treated in the same way as other components. For more details, see Paper I.

2.2 Improvements

The version of CHRONOSTAR described in Paper I has a number of computational bottlenecks that make it impractical to apply to the larger data sets required to model a large association such as Sco–Cen. First, the process of splitting groups into subgroups means that the total number of single component fits is $1 + \sum_{i=0}^{N_c} (N_c - i)(N_c - i - 1)$, where N_c is the total number of final components; for large N_c this sum scales as N_c^3. Secondly, the time required for each component fit is proportional to the number of stars.

To overcome these limitations, we have made the following key improvements to CHRONOSTAR, which do not affect the underlying formalism, but significantly improve speed:

(i) When carrying the likelihood maximization step in order to find the best-fitting parameters for each component, we have replaced the Markov chain Monte Carlo method used in Paper I with a simple derivative-free gradient descent algorithm (Nelder & Mead 1965); this locates the maximum significantly more rapidly.

(ii) When fitting multiple components, we parallelize the fit using multiple CPUs, so that we fit each component simultaneously using its own thread.

(iii) The version of the code described in Paper I integrated orbits (required for the trace-forward step) numerically. For ages <30 Myr, we replace this numerical integration with an analytic epicyclic approximation. We describe this in more detail in Appendix A.

3 FITTING SCO–CEN COMPONENTS

The process of fitting the N_c components and assigning membership probabilities to all stars in the vicinity of Sco–Cen has several steps. Aspects of this procedure are expected to change for future papers with even more speed improvements (e.g. further moving slow aspects of PYTHON code to C), but the general procedure for applying CHRONOSTAR to a new association or region of the sky remains as follows:

(i) Based on prior knowledge, define a region of six-dimensional (6D) kinematic space and specify data quality requirements in order to define a sample of stars.

(ii) After an initial fit, refine the association boundaries and initial conditions, and potentially refine the input catalogue.

(iii) Without re-fitting component properties, expand the input list of stars to those with lower quality data, and beyond the original 6D region.

The reasons for step (iii) are, first, that components inevitably extend beyond the original 6D region, so in order to include all their members we must extend them. Second, we have found that fitting components to stars with poor quality data increases both computational expense and the risk of producing artefacts; it is substantially more efficient to carry out an initial fit to determine component properties using only high quality data, and then extend the membership list to lower-quality data without re-fitting the individual components.

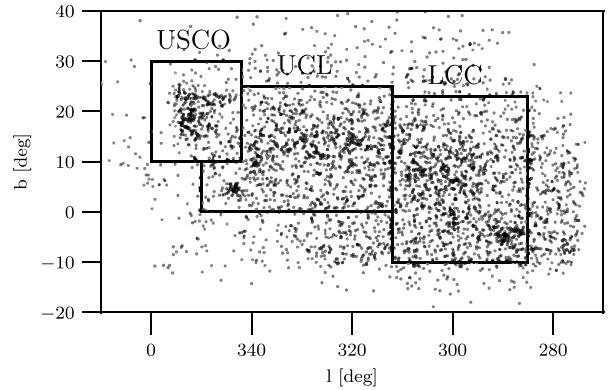For the fitting in this paper, we now describe the process as carried out for Sco–Cen.

Figure 1. Distribution in (l, b) of the 3,591 stars used in our initial fit of three subgroups (Section 3.1). The three boxes indicate the traditional boundaries of the Upper Scorpius (USCO), Upper Centaurus-Lupus (UCL), and Lower Centaurus-Crux (LCC) subgroups. ☊ .

3.1 Subsample definition and subgroup fits

Our initial sample was based on the Sco–Cen members from the BANYAN list (Gagné et al. 2018), which was based on the traditional boundaries of USCO, UCL, and LCC. We drew a 6D Cartesian box around all the stars in three subgroups, adding a margin of 30 pc and 5 km s^{-1} on each side and took all stars within those boxes from the 6D *Gaia* catalogue to make sure no new potential members were rejected. Stars were allowed to be assigned to more than one box due to overlapping margins. In total, only 3591 unique stars with 6D kinematic data from *Gaia* were included (excluding stars with missing radial velocities), with a two-dimensional (2D) distribution in l and b shown in Fig. 1. The median parallax uncertainty of the entire sample was 0.6 per cent with no stars exceeding 6 per cent. We included only stars with radial velocities, and the median radial velocity error for these stars was 1.37 km s^{-1}. Uncertainties of proper motions in right ascension (declination) were typically 0.07 (0.06) mas yr^{-1}.

In order to analyse the data using CHRONOSTAR, we transformed the observables for each star – right ascension, declination, parallax, proper motions and radial velocity – into Cartesian XYZUVW coordinates. In addition to central values, we transformed the uncertainties in the observable quantities into XYZUVW uncertainties using the Jacobian matrix given by Johnson & Soderblom (1987); multiplying the (diagonal) observable uncertainty covariance matrix by the Jacobian yields the (non-diagonal) XYZUVW covariance matrix.

The three subsets were fitted separately using CHRONOSTAR. The kinematic fits resulted in 22 unique components altogether, many of which account for non-homogeneous background.[2] Some components were discovered twice in neighbouring associations since the input data sets were slightly overlapping due to the wide cut-off boundaries.

3.2 Refined full-association fitting

To refine the fit, we merged together these 3591 stars and unique components from the three initial subsets and run a second CHRONOSTAR iteration on this limited subsample of stars. This fit was continued

---

[2]Our fit revealed that a single background component as described in Section 2.1 is not sufficient to describe all field stars.

until completion, i.e. until the BIC could not be improved by splitting any of the components further.

The refined fit converged with 19 components, where 6 of them again serve as background, and 6 of them are complex, meaning that they contain both old and young stars, they have large velocity dispersion at birth ($> 1 \, \mathrm{km \, s^{-1}}$) and occupy large volume in space. Ideally, the algorithm should have split these components further until all populations were separated, but either there kinematic data were insufficient to justify a further split, or the split became caught in a local minima (see Section 6). The remaining 7 components all have birth spatial dispersion less than 8 pc and velocity dispersion less than $1.1 \, \mathrm{km \, s^{-1}}$. The average velocity dispersion of $0.7 \, \mathrm{km \, s^{-1}}$ is consistent with velocity dispersions inferred from spatial distributions of young stars (Kraus & Hillenbrand 2008). These seven components are further subdivided into diffuse and dense components based on their birth velocity dispersion (less than or more than $0.7 \, \mathrm{km \, s^{-1}}$), which also correlates with their angular distribution on the sky. We present the fitted parameters in Table 1. Given the large number of parameters and that the split into subassociations is not likely to be unique, we do not derive formal uncertainties of the birth 6D positions or kinematic widths σ.

It is clear that in the future, expanding the input list of stars beyond the 3591 initially selected with full 6D *Gaia* kinematics may result in different and more complex fits. We make no orbital corrections for binary stars in this list. We further emphasize that our data selection is based purely on position in 6D parameter space, and completely neglects stellar age, location in the colour–magnitude diagram, or any other method of selecting young stars. For these reasons, we anticipate that future work will find significantly more substructure. However, these 13 non-background components still represent a rich data set to explore, especially when additional potential members are added from stars beyond the initial sample of 3591.

3.3 Expanded candidate list and membership probabilities

For the third step in our fitting procedure, we prepared a significantly new catalogue of candidate stars with lower quality data and extending significantly beyond the range of our initial fit, but did not re-fit the components with this larger input data set. The candidate stars were selected from the *Gaia* DR2 catalogue with the following requirements: $5 \, \mathrm{mas} < \mathtt{parallax} < 12 \, \mathrm{mas}$ (corresponding to distances between 80 and 200 pc), $\mathtt{parallax\_error} \leq 0.3 \, \mathrm{mas}$ that assures parallax errors smaller than 6 per cent at 200 pc (median parallax error in the entire sample is 1 per cent), $l > 240°$ or $l < 40°$, and $-60° < b < 70°$. Such selection results in 641 889 candidate stars, 127 228 of which have full 6D measurements available in the *Gaia* DR2 catalogue. This relatively small number of stars with full 6D measurements is because *Gaia* had a relatively bright magnitude limit for the radial velocity spectrograph, and also was not able to provide velocities for particularly hot or cool stars.

In order to maximize the probability of selection of potential members, this list was cross-matched with the external spectroscopic surveys via *Gaia* DR2 designation $\mathtt{source\_id}$ to obtain complementary radial velocity measurements. In total, we took measurements for 11 066 stars from the GALAH DR3 survey (Buder et al. 2021), 6554 from the RAVE DR6 list (Steinmetz et al. 2020), 4214 stars from the APOGEE DR16 list (Ahumada et al. 2020), 191 stars as tabulated in the Banyan Σ paper (Gagné et al. 2018), and 168 stars from Žerjal et al. (2021). If the star had multiple measurements in one of the external catalogues, we took the median value. In case the star had been found in more than one catalogue, the value with the smaller uncertainty was selected. Therefore, 15 597 radial velocities from the *Gaia* catalogue were replaced, and in total, 22 193

sources from the external catalogues are used. In total, 133 824 stars from our candidate list have a full 6D information available (21 per cent). As our fast overlap integral calculation requires a non-singular covariance matrix, we set the missing radial velocity values to $0 \pm 10\,000 \, \mathrm{km \, s^{-1}}$. Such large uncertainties result in the stellar covariance matrices resembling a highly elongated ellipsoids and give membership probabilities indistinguishable from those with formally missing radial velocities.

In the final step we compute the overlap integrals between the components and the stars themselves. Essentially, this is the expectation step from CHRONOSTAR's algorithm used with the new larger data set. These overlaps are then normalized such that the sum of the membership probabilities for each star equals unity. This takes into account all components from the model, including background components. A full list of stars with their membership probabilities greater than 50 per cent to all non-background components is provided in Table C1 together with their radial velocities. Each member can only be assigned to one of the components with membership probability greater than 0.5.

Although our model is based on the input sample covering a parameter space smaller than the expanded candidate list, it adequately represents the association. For example, Fig. 2 shows that Sco–Cen components are centred within the traditional boundaries of the association. Stars outside of the traditional boundary of the association lie in the outskirts of Sco–Cen and in the tails of the multidimensional Gaussian models of components. The exception is component E, which incorporates a significant number of stars outside the parameter space used in the fit.

The distribution of membership probabilities for each of the non-background components typically has a U-shape, with most of the stars having probabilities either close to 0 or close to 1. In particular, 8 Sco–Cen components consist of 8185 stars with membership probability greater than 0.5, and 4511 stars with 90 per cent or higher membership probability.

3.4 Stellar age uncertainties

Age uncertainties $\Delta T_{\mathrm{birth}}$ as listed in Table 2 are determined as the ratio of σ_{X_0} and σ_{V_0} from Table 1, which represents a kinematic crossing time for stars within the association at birth. Individual stars in the association are not expected to have ages that are more uniform than $\Delta T_{\mathrm{birth}}$, unless the stars are part of subassociations.

Seven of the components have birth crossing times at birth shorter than their age, which suggests that the age estimates are meaningful and non-zero. For these components, the velocity dispersions at birth are also similar to isothermal sound speeds in young associations, meaning that these age uncertainties provide a realistic estimate for the dynamical time-scales over the spatial scales defined by the associations. More refined kinematic estimates could only be obtained by further resolving substructure.

Several dense components (D, H, and I) are potentially gravitationally bound. This contradicts CHRONOSTAR's assumption that stars move ballistically through the Galaxy, and means that our kinematic ages are likely to be underestimated. Physically, this is simply because a bound group of stars remain coherent in phase space far longer than would be expected for stars on ballistic orbits; since we do not account for this effect, CHRONOSTAR interprets tight clustering in phase space as young age. Consistent with this analysis, the kinematic ages we obtain for components D, H, and I are much smaller than the values from the alternative techniques such as isochronal fitting and lithium depletion boundary age and have large uncertainties. They are not reliable estimates, but are none the less reported for completeness.

Table 1. Components in the Sco–Cen model today (time t) and at birth (time 0). All velocities are with respect to the LSR (see Section 2) and not the Sun. Components are split into four different types based on their structure and stellar population. Velocity dispersion is, with a few exceptions, a good indicator of the nature of the component. Diffuse components on average have larger velocity dispersions than dense components; dense components are likely gravitationally bound. Complex components encompass multiple or older populations (including pre-main sequence stars) as determined by the colour magnitude diagram, not used by CHRONOSTAR directly. Columns T_{age} and ΔT_{birth} provide kinematic age and crossing-time, while N_{fit} gives a number of stars used in the fit. Full table (including full covariance matrices) is available online as Supplementary Material.

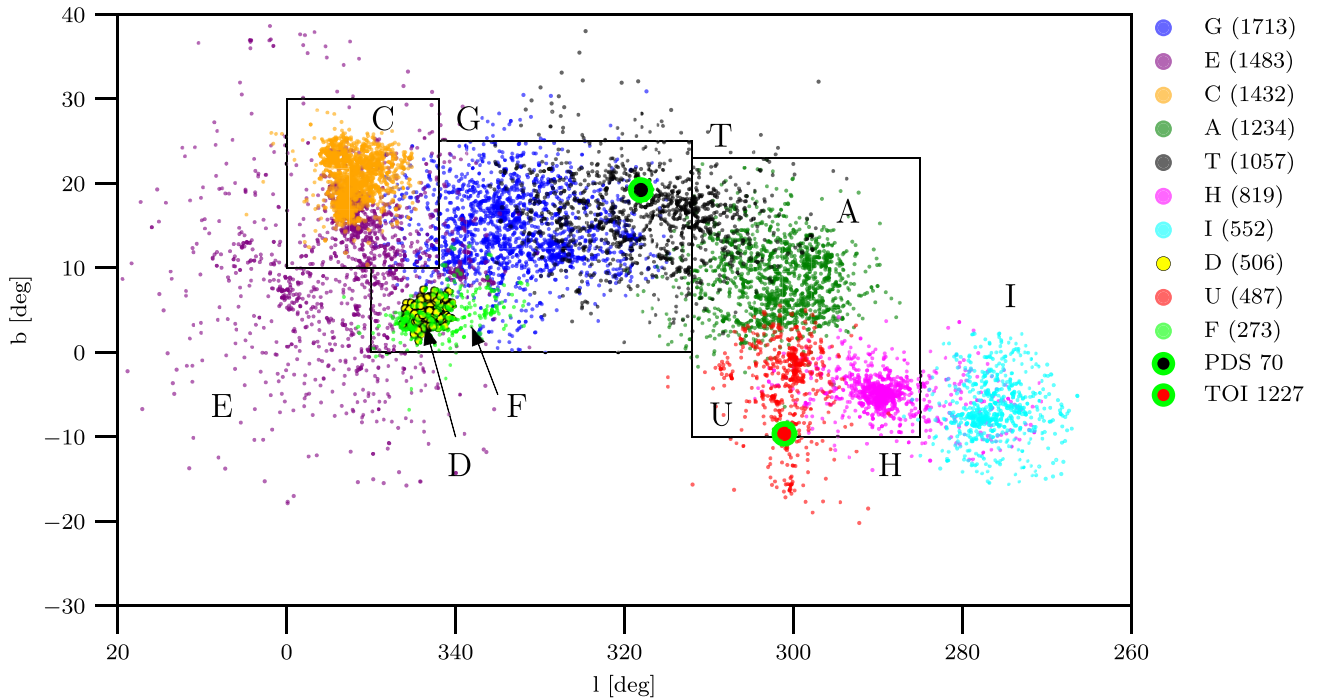| ID	X_t (pc)	Y_t (pc)	Z_t (pc)	U_t (km s⁻¹)	V_t (km s⁻¹)	W_t (km s⁻¹)	σ_{X_t} (pc)	σ_{Y_t} (pc)	σ_{Z_t} (pc)	σ_{U_t} (km s⁻¹)	σ_{V_t} (km s⁻¹)	σ_{W_t} (km s⁻¹)	X_0 (pc)	Y_0 (pc)	Z_0 (pc)	U_0 (km s⁻¹)	V_0 (km s⁻¹)	W_0 (km s⁻¹)	σ_{X_0} (pc)	σ_{V_0} (km s⁻¹)	T_{age} (Myr)	ΔT_{birth} (Myr)	N_{fit}
Diffuse components																							
A	60	−95	42	2.7	−8.7	0.8	10	10	9	1.1	1.1	0.9	34	−37	30	0.6	−9.4	2.3	6	1.1	7	5	153
T	98	−87	64	4.9	−7.8	1.5	17	16	13	1.1	0.9	0.5	43	28	5	0.2	−9.3	5.0	3	1.0	15	3	128
U	54	−91	19	1.4	−7.6	−0.8	7	7	6	0.7	0.7	0.5	38	−26	21	−1.1	−8.0	0.3	3	0.7	9	4	54
Dense components																							
D	168	−50	39	7.0	−7.3	3.0	3	3	3	0.3	0.3	0.3	151	−44	32	6.2	−7.7	3.5	3	0.3	2	7	46
F	169	−58	36	9.7	−8.8	3.1	10	10	8	0.7	0.6	0.3	64	58	−22	3.8	−11.7	3.8	1	0.6	15	2	16
H	48	−143	12	2.6	−9.4	6.2	11	10	6	0.4	0.4	0.6	13	3	−70	−1.9	−10.4	3.4	8	0.4	15	21	84
I	18	−133	8	0.0	−10.1	3.3	6	6	6	0.5	0.5	0.5	11	−111	1	−0.6	−10.2	3.3	6	0.5	2	11	35
Complex components																							
B	122	−36	60	6.2	−6.4	1.9	22	22	21	1.9	1.8	1.8	91	−16	47	4.8	−7.3	3.4	20	1.9	5	11	296
C	133	−19	76	5.2	−3.5	−0.9	7	7	7	1.2	1.2	1.2	113	−17	76	4.3	−4.1	0.8	5	1.2	4	4	130
E	129	−22	52	7.9	−4.2	0.7	19	18	16	1.7	1.5	1.1	54	10	28	5.4	−6.3	3.4	6	1.6	11	4	94
G	116	−59	59	6.9	−8.5	2.8	16	15	12	1.1	0.9	0.8	49	40	2	2.5	−10.3	5.3	8	1.0	13	8	167
J	62	−94	36	3.0	−9.6	2.0	28	26	21	1.7	1.6	1.6	34	−2	7	−0.3	−10.4	3.3	21	1.6	10	12	197
Q	59	−156	35	−13.1	−3.3	−0.1	24	24	23	4.9	4.9	4.9	70	−154	35	−13.3	−3.0	0.2	23	4.9	1	5	212
Background components																							
K	105	−126	45	−22.9	−3.0	−5.7	27	27	27	2.8	2.8	2.7	145	−128	56	−23.3	−2.0	−5.1	26	2.8	2	9	77
L	89	−184	31	−21.2	−5.6	5.8	37	34	26	2.1	1.9	2.1	289	−209	−38	−24.1	−0.2	5.5	28	1.9	11	14	37
M	93	−95	53	−12.4	−7.8	6.4	33	32	30	2.4	2.3	2.3	159	−75	10	−14.3	−6.0	7.6	30	2.3	6	12	116
N	49	−90	39	−18.9	−2.1	0.7	22	22	22	4.7	4.7	4.7	51	−90	39	−18.9	−2.1	0.7	22	4.7	0	5	245
R	123	−99	41	−23.4	−1.6	3.6	25	25	25	2.6	2.6	2.6	127	−99	40	−23.5	−1.5	3.7	25	2.6	0	10	93
S	126	−102	47	−11.8	−2.3	0.5	31	31	31	4.0	4.0	4.0	126	−102	47	−11.8	−2.3	0.5	31	4.0	0	8	210

Figure 2. Components of the Scorpius–Centaurus association and its immediate neighbourhood, as described with the kinematic model from CHRONOSTAR. There are 9556 stars in this plot, which shows all stars with membership probabilities at least 50 per cent in one of the 10 components indicated. The numbers of members for each component are shown in the legend; stars are assigned to the component for which the membership probability is highest. Black lines denote the traditional split into the three regions of the association USCO, UCL, and LCC. Exoplanetary hosts PDS 70 and TOI 1227 are members of components T and U, respectively. ⊘ .

Table 2. Number of members in individual components with membership probabilities above 0.5, 0.8, and 0.9. Total number includes all stars in Sco–Cen components except B, which is composed of young and dominantly old populations of stars. Components H (IC 2602) and I (Platais 8) are not part of the association. ⊘ .

ID	Members			T_{age}	ΔT_{birth}
	$p > 0.5$	$p > 0.8$	$p > 0.9$	(Myr)	(Myr)
USCO components					
C	1432	1246	1106	4	4
E[a]	1483	949	678	11	4
UCL components					
D	506	416	349	2	7
F	273	197	169	15	2
G	1713	1023	633	13	8
T	1057	747	590	15	3
B[a]	4385	2344	1444	5	11
LCC Components					
A	1234	846	610	7	5
U	487	408	376	9	4
Total	8185	5832	4511		
Known clusters					
H	819	785	759	15	21
I	552	491	445	2	11

Note.[a]Complex, multipopulation component.

4 RESULTS

Our results from CHRONOSTAR provide a kinematic decomposition of Sco–Cen that does not rely on any kinematic or evolutionary filters. The kinematic model that best describes the input 6D data set of

the Scorpius–Centaurus region in this work is composed of 13 non-background components. We plot the (l, b) positions of all identified stars with membership probabilities of more than 50 per cent in Fig. 2; colour indicates the highest-probability component assignment for each star. The figure reveals the familiar outline of the association including its complex substructure with both dense and diffuse groups, but also includes components that go beyond the traditional boundaries of USCO, UCL, and LCC (e.g. component E) and that include clusters (IC 2602 – component H and Platais 8 – component I). Component populations range from a few hundred (component F) to almost 2000 (component G), and many of them feature further substructure. The total number of stars in each component with membership probability greater than 0.5 is presented in Table 2. There are 329 stars that do not meet the membership criteria in this table, but the sum of their membership probabilities for Sco–Cen components is greater than 0.5. In such cases, their membership is distributed between at least two Sco–Cen components.

Our kinematic analysis has yielded a reliable extraction of young stars from an unbiased data set, based solely on their common motion through space. We emphasize that the majority of stars (80 per cent) lack radial velocities, but they are nevertheless constrained well enough in the remaining 5D to yield significant overlaps with the Sco–Cen model components. We discuss the contamination rate in our analysis in Section 5.2. Because there is no kinematic discrimination in the input catalogue, CHRONOSTAR reconstructs all major kinematic groups in the data regardless of their origin or connection to Sco–Cen. We thus note that not all substructures are necessarily related to the Scorpius–Centaurus association. We discuss the individual components below and validate their kinematic ages in Section 5. At various points, we provide colour–magnitude diagrams for different components; all of these are dereddened, using
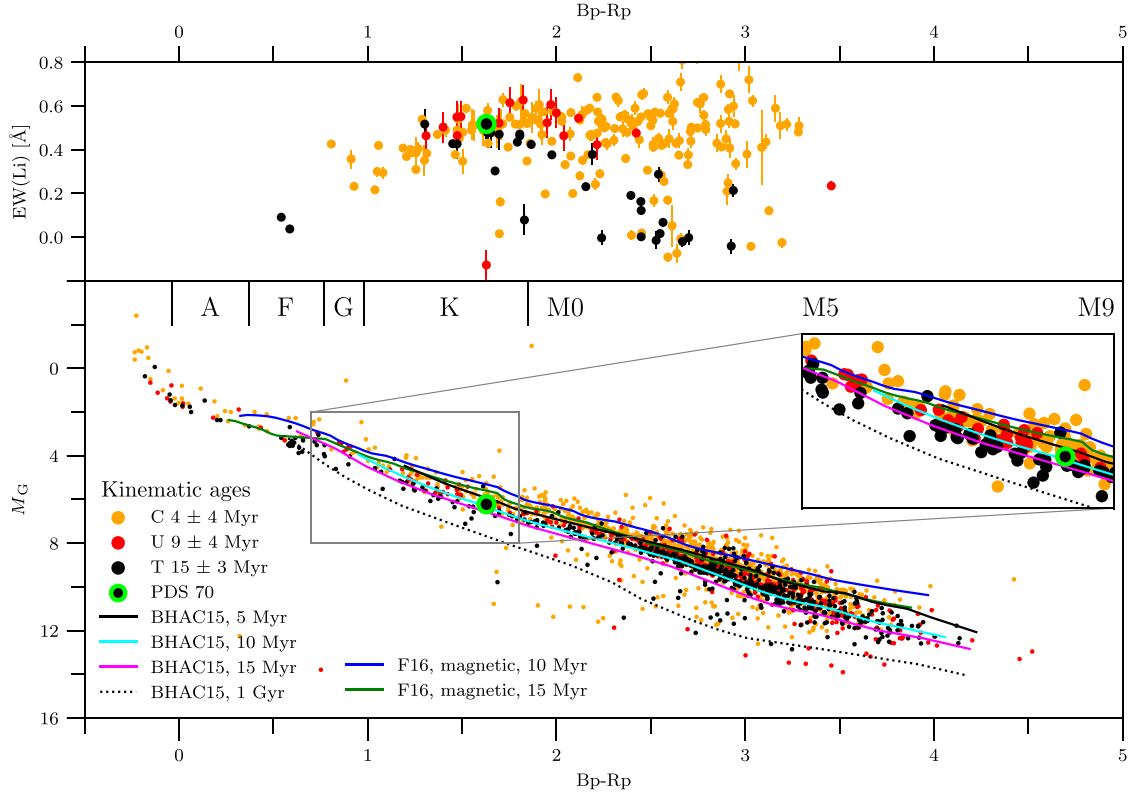
Figure 3. *Lower*: A *Gaia* $M_G - (B_p - R_p)$ colour–magnitude diagram of our candidates in components C, U, and T with membership probability greater than 90 per cent. Component *T* is kinematically the oldest component (15 ± 3 Myr) and shows lower overluminosity and lithium strength than kinematically younger components U and C. The kinematic age of component U is 9 ± 4 Myr, but its lithium strength does not show a significant difference with component C; the latter is likely composed of multiple populations with an age spread. An equal mass binary sequence is clearly present in the component *T*; the exoplanetary host PDS 70 belongs to this component. For reference, we overplot Baraffe et al. (2015, BHAC15) models and isochrones with magnetic fields from Feiden (2016, F16). *Upper*: EW(Li) measurements for candidates as a function of *Gaia* $B_p - R_p$. ☍ .

the reddening correction procedure described in Appendix B, but the average extinction for most of the components is very small (<0.2 mag, Table B1). Thus, comparisons between the components and theoretical isochrones are not affected by reddening. Components C, D, and F are an exception to this statement, and have relatively large extinction ($0.4-0.6$ mag). This is consistent with previous work showing that Upper Scorpius, described by the component C (discussed below in Section 4.3), has a large extinction (e.g. de Geus, de Zeeuw & Lub 1989).

4.1 Components G and T: Upper Centaurus-Lupus

Within the region that corresponds to Upper Centaurus-Lupus, CHRONOSTAR identifies two major components, G and T, with 1713 and 1057 probable members, respectively. Their colour–magnitude diagrams (Figs 3 and 4) show that the stars we identify as belonging to these components lie well above the main sequence, confirming their youth. The figures also reveal a significant number of equal-mass M dwarf binaries in both components. A large number of stars in this binary sequence have ruwe>1.5, as is typical for binaries. Although their spatial distribution shows complexity beyond a simple split into two groups [i.e. the Lupus complex, e.g. Hara et al. (1999) and the two filaments of the T component that continue into the component A], stars of both parts show similar distance distributions (Fig. 5), ranging from 100 to 170 pc with centres at ∼135 pc (T) and ∼145 pc (G).

The shape of both model components taken together is approximately an oblate spheroid with a 15 pc semi-axis in the *Y*-direction,

and 5 pc in the orthogonal directions. While the elongated shape of the UCL alone might have forced CHRONOSTAR to split it into two parts, components T and G also show slightly different kinematic properties. The G component appears to be moving faster towards the Galactic centre since its U velocity at birth ($2.5\,\mathrm{km\,s^{-1}}$) is significantly higher than for the T component ($0.2\,\mathrm{km\,s^{-1}}$). This difference is significant, since the dispersions within each component are only $1\,\mathrm{km\,s^{-1}}$. Taken together, these two components could be modelled as a rotating elongated ellipse at birth.

4.2 Components A and U: Lower Centaurus-Crux

LCC is comprised of two kinematically distinct groups A and U, with 1234 and 487 members, respectively. Component U extends to the south towards the region in the sky where ϵ Cha is found at (l, b) ≈ (300, −16) deg. It includes 3 stars from the Murphy, Lawson & Bessell (2013) list of ϵ Cha members.

The model velocity dispersion of the U component ($1.0\,\mathrm{km\,s^{-1}}$) is similar to those of the dense components (Table 1). This is perhaps not surprising as there is an overdensity of stars in the northern part at (l, b) ≈ (300, 0) deg. Goldman et al. (2018) report a new large moving group in the LCC composed of four kinematic subgroups. Their groups A0 and A are fully contained in our component U (195 stars), while only 86 per cent (698 stars) of the members of their groups B and C were found to belong to CHRONOSTAR's component A. Members of their group Z are distributed between our components A, U, and J.
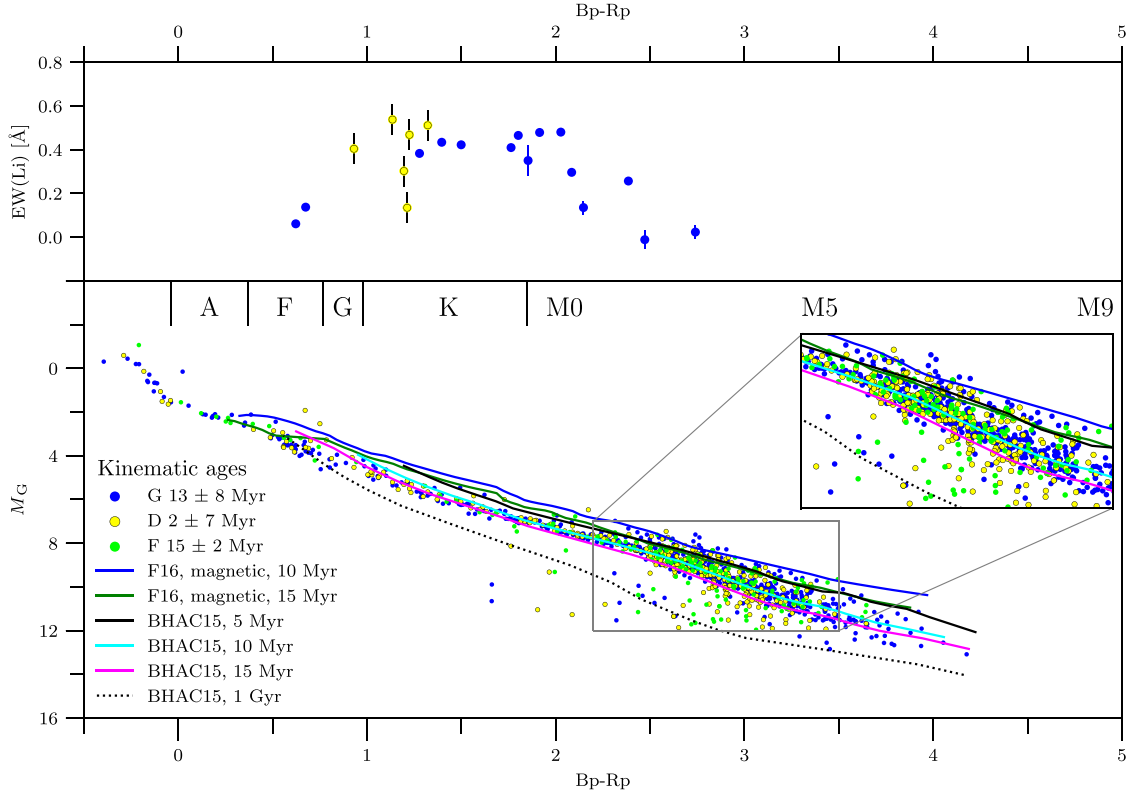
Figure 4. *Lower*: A *Gaia* $M_G - (B_p - R_p)$ colour–magnitude diagram of our candidates in components G, D, and F with membership probability greater than 90 per cent. All three components show similar overluminosities. An equal mass binary sequence is visible in all of them. *Upper*: EW(Li) measurements for candidates as a function of *Gaia* $B_p - R_p$. ⟳ .
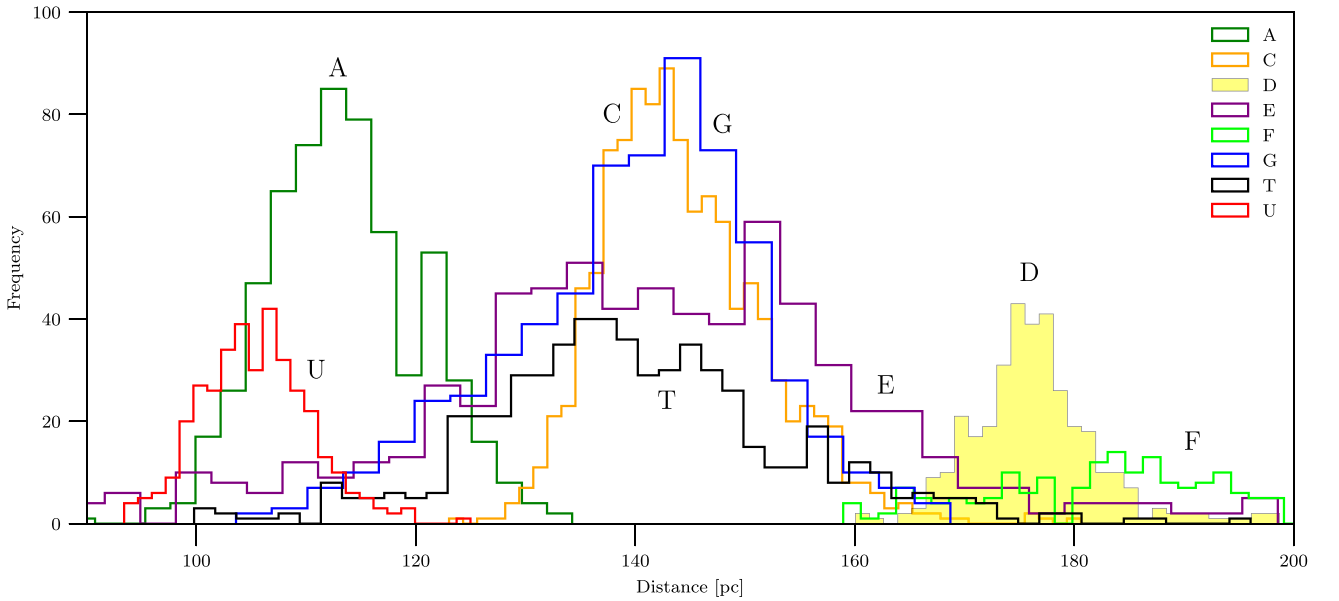

Figure 5. Distance distribution for stars with Sco–Cen membership probability $p > 0.9$. While components G and T (both in the UCL region) have similar distance distributions, it turns out that component U lies ∼10 pc closer than A (both in LCC). Component C (USCO) has an average distance similar to G, but it is skewed towards larger distances. Components D and F overlap in the sky, but F appears to be slightly more distant. Component E is double-peaked with the more distant peak overlapping with USCO in the sky. Stars from the peak at ∼135 pc are distributed over the USCO and south of this region down to $b \approx 0$ deg. Bin sizes are different for different components in order make it possible to visualize components with very different total memberships on the same plot. ⟳ .
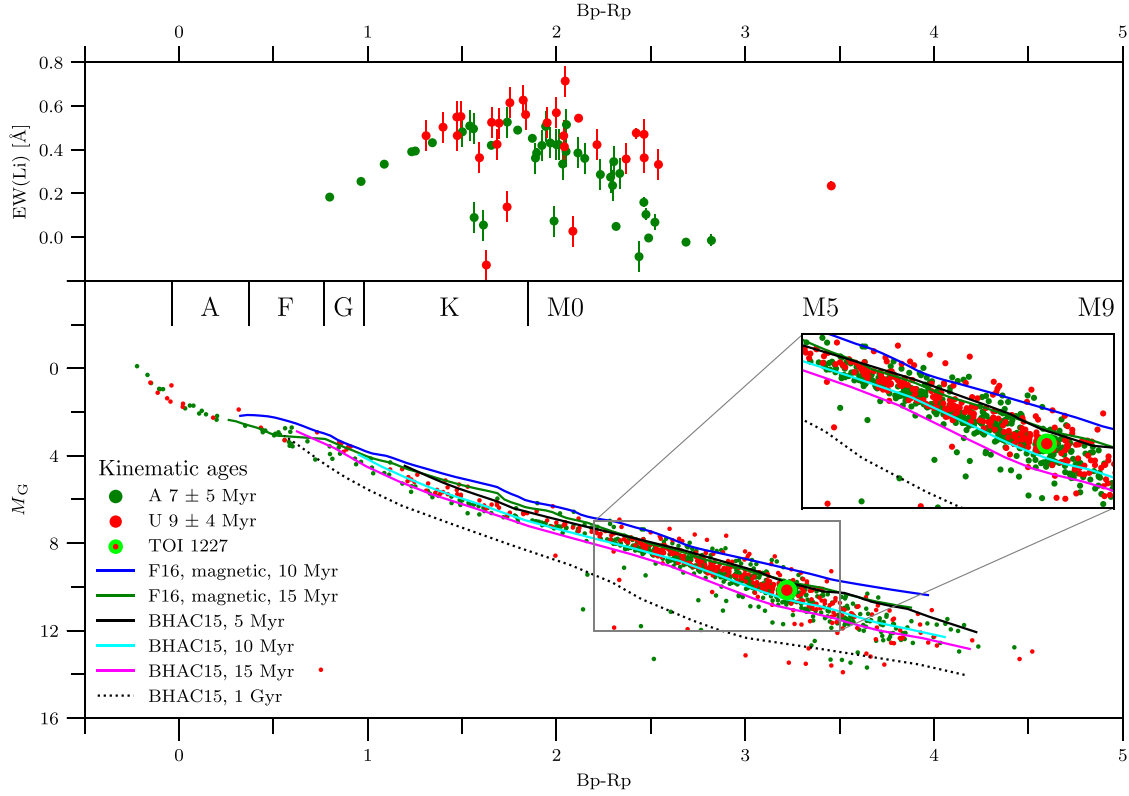
Figure 6. *Lower*: A *Gaia* $M_G - (B_p - R_p)$ colour–magnitude diagram of our candidates in components A and U from LCC with membership probability greater than 90 per cent. Their kinematic ages are the same within their uncertainties, but component U appears to be slightly younger than A based on its lithium strength. The inset shows the equal mass binary sequence in both components. An exoplanetary host TOI 1227 belongs to component U. *Upper*: EW(Li) measurements for candidates as a function of *Gaia* $B_p - R_p$. ⟳ .

Despite the partial overlap of components T and A in the sky, Fig. 5 demonstrates that the majority of stars in A are located ∼20 pc closer. This is a sparse component with a large velocity dispersion (1.8 km s^{-1}).

A colour–magnitude diagram shows the young age of both components and reveals that component U is likely younger than component A (Fig. 6). Age is discussed in more detail in Section 5.

4.3 Component C: Upper Scorpius

The most studied part of the Sco–Cen association – Upper Scorpius – is described with the component C comprising 1432 members. A cross-match with the list of 1342 members from Luhman & Esplin (2020) that have parallax_error < 0.3 mas shows 891 stars in common with C (membership probability >0.5), and additional 373 stars from components E and B.

This is a complex component in the CHRONOSTAR model, consistent with the growing observational evidence for multiple populations in USCO (e.g. Kerr et al. 2021; González et al. 2021; Squicciarini et al. 2021). It likely consists of multiple populations that have not been recovered within this model due to the limitations of the input catalogue to the fit. This claim is supported by the relatively large velocity dispersion of 1.2 km s^{-1} in each dimension (Table 1) and a large luminosity spread of about 2 mag for M0 dwarfs, which is a few times wider than for the T component (about 0.6 mag; Fig. 3). This might result from component C being affected by a large extinction (median value of 0.62 mag and standard deviation of 0.42 mag) and containing multiple populations of different ages.

On the other hand, the distance distribution for C does not reveal any distinct overdensities.

4.4 Component E

The diffuse part of the association between Upper Scorpius and Corona Australis is described by component E, which also overlaps significantly with the Upper Scorpius region and partly the Lupus complex in the sky. This is one of the complex and poorly constrained components because the majority of its members lie outside of our input data to the fit (see Section 3.3). Its colour–magnitude diagram (Fig. 7) shows a double sequence where the younger sequence comes from the Lupus overdensity. Likewise, its distance distribution (Fig. 5) shows two major peaks. Stars from the more distant peak lie slightly behind the southern part of USCO, while objects from the nearer peak are more evenly distributed in the sky. An overdensity at (l,b) ≈ (0,7) deg contains 46 out of 48 stars from the group Theia 67 identified by Kounkel & Covey (2019).

4.5 Components F and D: V1062 Sco

One of the most compact components of the model, component D, corresponds to the group V1062 Sco that was recently discovered by Röser et al. (2018). The authors report 63 comoving stars with ages from less than 10 to about 25 Myr. Our component D contains 33 members from their list, component F 6 members and component B 10 members. However, we find that component D contains many more stars than Röser et al. (2018) study: 506 stars above the 50 per cent membership probability threshold.
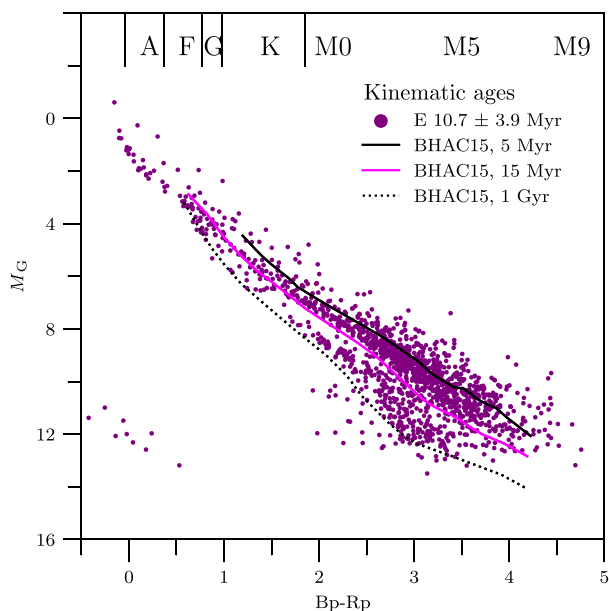
Figure 7. A *Gaia* $M_G - (B_p - R_p)$ colour–magnitude diagram of our candidates in component E with membership probability at least 50 per cent. This is a complex and poorly constrained component because the majority of its members lie outside of our input data to the fit. Its colour–magnitude diagram shows a double sequence. ⟳ .

CHRONOSTAR assigns component D a kinematic age of 2 Myr, but the large associated uncertainty of ±7 Myr makes this estimate highly unreliable; the component is dense and likely gravitationally bound, invalidating the central assumption of CHRONOSTAR's kinematic aging method. This concern is consistent with a direct estimate of boundedness: the virial mass sum of component D (neglecting factors of order unity) is ∼150 M$_\odot$, significantly less than the total cluster mass. Moreover, the colour–magnitude diagram for this component (Fig. 4) demonstrates an overlap with the component T again suggesting that kinematic analysis underestimates its age. The median distance derived of the members is 176 pc, which compares well with 175 pc as found by Röser et al. (2018).

Component F, which is described as SC 14 in Kerr et al. (2021), is located in the same line of sight as D, but is more diffuse with no clear peak in the distance distribution. Its stars are found between 160 and 200 pc. Despite the fact that the number of stars used in the fit was relatively low (16; Table 1), its kinematic age 15 ± 2 Myr seems to roughly compare with that of component T and is consistent with the isochronal age (14.1 ± 1.2 Myr) from Kerr et al. (2021).

4.6 Components H and I: IC 2602 and Platais 8

In addition to V1062 Sco, CHRONOSTAR also identifies two other known open clusters: components H (IC 2602) and I (Platais 8). The sequences in the colour–magnitude diagram for both clusters are narrow, except for M dwarfs where the contamination rate is higher (Fig. 8). A cross-check with Dobbie, Lodieu & Sharp (2010) revealed that 11 out of 17 stars in their list of IC 2602 members have 100 per cent membership probability in component H, which contains a total of 819 members in our model. Component I has 552 members, 6 of which are in common with Gagné et al. (2018)'s list of 11 stars from Platais 8 (Platais, Kozhurina-Platais & van Leeuwen 1998). The median distance of Platais 8 in this work is 143 pc.

As for the D component, we regard CHRONOSTAR's kinematic ages for these components unreliable due to their high density and potential gravitational interactions; consistent with this concern, the ages we recover have very large uncertainties. IC 2602 has a reported lithium depletion boundary age of 46^{+6}_{-5} Myr (Dobbie et al. 2010) while the age estimate for Platais 8 is 79 Myr with a large uncertainty (Yen et al. 2018).

4.7 Background and components B, J, and Q

Although CHRONOSTAR's model incorporates a component that is associated with the background from the very beginning, its component splitting method introduced 6 additional components K, L, M, N, R, and S that typically consist of thousands of stars but completely lack young stars in the colour–magnitude diagram. They have large velocity dispersions and a very young age; the latter is required because it is impossible for such a kinematically incoherent group of stars to stay together for a long time. We denote these as background components (see Table 1). The most likely explanation for the introduction of this components is that the stellar background (i.e. stars not kinematically associated with the moving group) is not as homogeneous as CHRONOSTAR assumes, and that the fixed amplitude for CHRONOSTAR's background is not high enough.

There are three dominant background but complex components in the model: B, J, and Q, consisting of 15 432 members in total. They are centred on the outskirts of the association and are not well constrained due to the poor coverage of the parameter space outside the traditional Sco–Cen boundaries in the input catalogue. Most of these stars are old background objects, but Fig. 9 reveals a substructure that corresponds to some of the known groups of young stars. Their colour–magnitude diagrams confirm the presence of a very young population of stars above the main sequence. These overdensities might be part of the known groups or might represent standalone components that would be recovered with a more populous input catalogue. At the same time, it is likely that the large background components stole some of the members of the more diffuse components of the Sco–Cen association. Further fitting would help to answer these questions.

A further cross-check with the literature confirms membership of 299 of 313 stars reported to be in the Corona Australis association by Galli et al. (2020). These authors found that the association appears to be more complex and is composed of two kinematically and spatially distinct subgroups with stars younger than 10 Myr. Additionally, our cross-check with the list from Gagné et al. (2018) confirms that our component B contains 7 X-ray sources from Neuhäuser et al. (2000) that lie in between Corona Australis and Upper Scorpius, and belong to the Upper Corona Australis in the Banyan Σ model.

Other known young clusters and associations covered by the background components are IC 2391, Platais 9, the ε Chamaeleontis star-forming complex (Murphy et al. 2013) that is split into Cha I and Cha II in (Galli et al. 2021). Component Q consists of 167 stars belonging to Cha I and 33 found in Cha II in their list. This is a very young complex, with an age estimated to be 1–2 Myr (Galli et al. 2021).

5 DISCUSSION

5.1 Kinematic ages versus ages derived by other methods

Kinematic ages are based on the assumption that resolved associations are gravitationally unbound and thus expanding. Stars in an
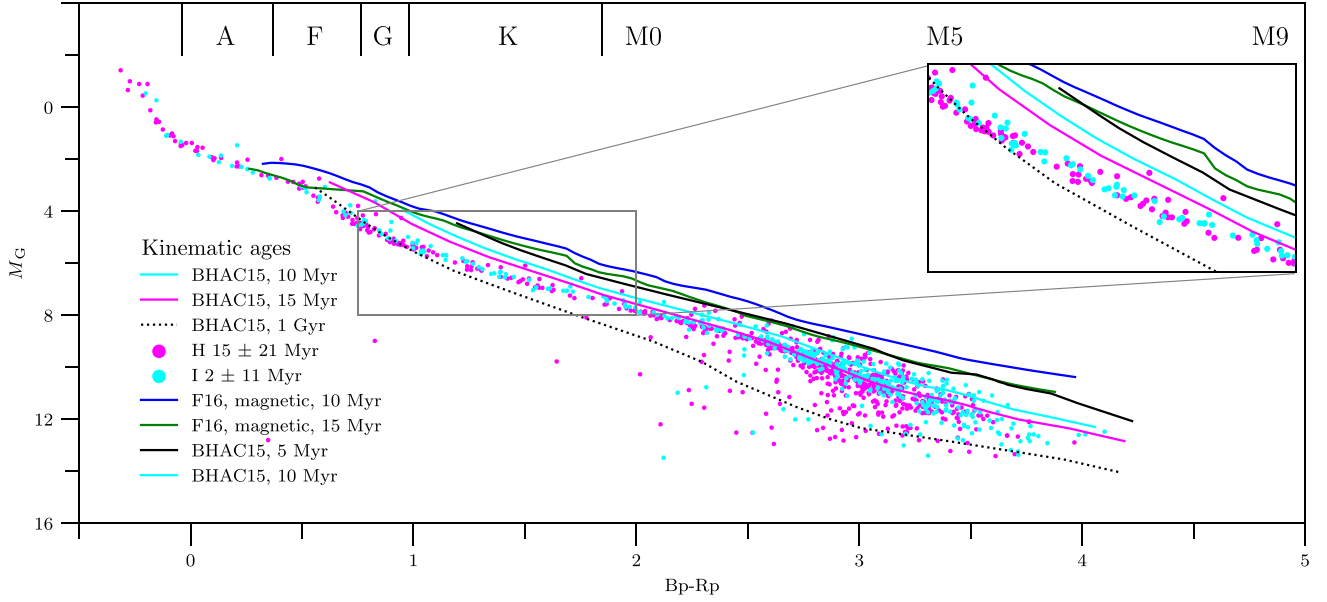
Figure 8. A *Gaia* $M_G - (B_p - R_p)$ colour–magnitude diagram of our candidates in components H and I corresponding to clusters IC 2602 and Platais 8, respectively. Their sequences are narrow and lie lower in the diagram than the rest of the components due to their older age (~50 Myr). ☊ .
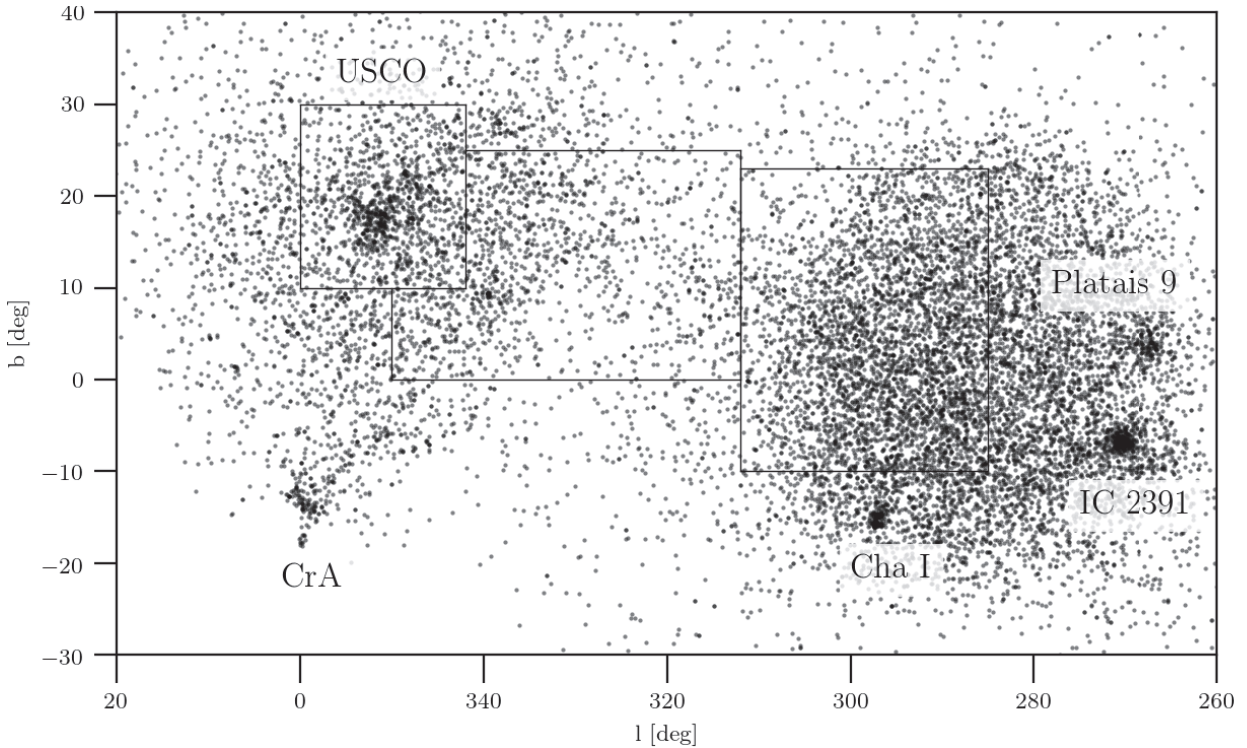

Figure 9. Components B, J, and Q from the model are complex and cover a very large volume. Out of their 15 432 members, most are old stars and belong to the background. Due to their expanse, however, they also cover some of the overdense groups of stars, e.g. Corona Australis (CrA), Chamaeleontis I (Cha I), Upper Scorpius (USCO), IC 2391, and Platais 9. ☊ .

association share their common motion through space and follow ballistic orbits around the Galaxy. The model in CHRONOSTAR uses this picture to assign ages, by searching for an initial distribution (in 6D phase space) and age such that, when the distribution is propagated forward by the modelled age of the component, it matches the 6D phase space distribution for that component which we observe today. Due to the presumption that the expansion begins immediately

after the birth of the association and not later, the model provides the lower age limit of the group.

Given the unavoidable assumptions behind this technique, it is important to cross-check kinematic ages against those derived from other methods, which carry their own assumptions and uncertainties. One cross-check to which we have already alluded is to ages derived from colour–magnitude diagrams. Fig. 3 compares colour–
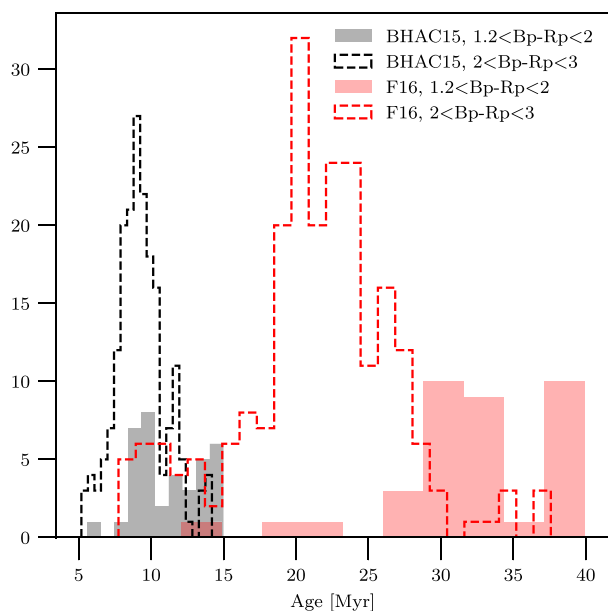
Figure 10. Distribution of ages derived from the interpolation of the colour–magnitude positions of stars from the component T. We used isochrones from Baraffe et al. 2015 (BHAC15, 5–15 Myr) and magnetic models from Feiden 2016 (F16, 5–40 Myr) and excluded stars outside these age ranges. We split the sample into two colour ranges corresponding to K and early M dwarfs (1.2 < Bp-Rp < 2 and 2 < Bp-Rp < 3, respectively). Both models and colour ranges give different ages. ⟳ .

magnitude diagrams of three components with a range of kinematic ages: component T (15 ± 3 Myr), U (9 ± 4 Myr), and C (4 ± 4 Myr; this is the youngest component (USCO) based on the isochronal fits from the literature, but it is non-trivial to interpret; see Section 5.1.2). The trend of decreasing overluminosity with kinematic age is clear, and is also consistent with the relative difference in lithium strength between components T and C. Thus we find a comforting qualitative consistency between the relative ages that CHRONOSTAR derives from kinematics and the relative ages one would infer from both colour–magnitude diagrams and lithium depletion.

To make this comparison more quantitative, in Fig. 3 we overplot Baraffe et al. 2015 (BHAC15) isochrones for 5, 10, and 15 Myr, as well as magnetic isochrones from Feiden 2016 (F16); we have converted the latter to *Gaia* photometry using the colour–temperature and luminosity–log *g* relations from Pecaut & Mamajek (2013) based on an online version of their table.[3] Besides the uncertainty introduced by this conversion and the fact that these relations are provided for the main sequence stars while magnetic isochrones are computed for young ages, neither of the Baraffe et al. (2015) isochrones matches the G or K stars perfectly either. For example, F and G stars from the component T are best described with the 15 Myr isochrone while a 10 Myr isochrone appears to be a better fit for K and M dwarfs. Using isochrones from BHAC15 and magnetic models from F16, we interpolated the colour–magnitude positions of stars in component T onto ages in two colour ranges corresponding to K and early M dwarfs (1.2 < Bp-Rp < 2 and 2 < Bp-Rp < 3, respectively). The resulting age distributions show age difference between the spectral types and models (Fig. 10). The magnetic and non-magnetic models give ages that differ for more than 10 Myr. This is well

beyond the already naturally large age spread of the populations due to the often large birth kinematic or sound crossing timescales for the associations. The phenomenon of mass-dependent ages has been consistently observed in Sco–Cen (e.g. Pecaut, Mamajek & Bubar 2012; Kraus et al. 2015; Rizzuto, Ireland & Kraus 2015; Pecaut & Mamajek 2016) and in the Taurus association (Gully-Santiago et al. 2017; Rizzuto et al. 2020). Several suggestions have been proposed to account for this discrepancy, from undetected binary stars (Sullivan & Kraus 2021), starspots (Somers & Pinsonneault 2015), magnetic fields (Feiden 2016) to insufficient evolutionary models of pre-main sequence M dwarfs (Jeffries et al. 2017; Rizzuto et al. 2020).

Lithium depletion ages suffer from significant model uncertainties. As summarized by Binks et al. (2022), the main problems include an underestimated lithium depletion at an age that best describes the position of pre-main sequence stars in the colour–magnitude diagram from the same model isochrones. An inclusion of surface magnetic fields and starspots provides a better agreement between the isochronal and lithium depletion age but suggests significantly older ages than predicted by the standard model isochrones. Additionally, lithium depletion in standard models occurs at temperatures much hotter than observed (e.g. λ Orionis and γ Velorum; Binks et al. 2022) and seems to correlate with rotation in some young clusters (e.g. NGC 2516) but not in others (e.g. γ Velorum). This makes it much more difficult to be quantitative in the same way we have attempted for isochrones.

In the remainder of this section we make more detailed comparisons between our kinematic ages and previously-published literature estimates. We focus here on the components with the most well-determined kinematic ages (G, T, A, U, and C), excluding fits based on very few stars (F), complex components for which a single kinematic age is dubious (B, E, J, and Q), and collections of stars that are likely bound and thus fail to satisfy the basic assumption of kinematic aging (D, H, and I).

5.1.1 Age of UCL: components T and G

CHRONOSTAR's kinematic age for component T is 15 ± 3 Myr. The model is fit on 76 stars with measured radial velocities; most are FGK or early M-type dwarfs. Based on the colour–magnitude diagram shown in Fig. 3, this component has a relatively small spread in luminosity (∼0.6 mag for M0 dwarfs), likely indicating a small age spread. Comparison of the stars in this component to Baraffe et al. (2015) isochrones gives an age of 7–15 Myr for K and 5–13 Myr for M dwarfs (Fig. 10). The kinematic age of the K dwarfs is consistent with the isochronal estimate and the main-sequence turn-off age of 17 ± 1 Myr obtained by Mamajek, Meyer & Liebert (2002), while no agreement exists for M dwarfs. Thus, our result represents the first kinematic age derived for the K dwarfs of the Upper Centaurus-Lupus association that agrees with age estimates from stellar evolution.

Our kinematic age estimate for component G is 13 ± 8 Myr. Thus our central estimate of the age of this component is similar to that for component T, which is consistent with our finding that the two components overlap substantially in the colour–magnitude diagram. However, component G also shows a small dispersion in luminosity along the sequence (comparable to component T; Fig. 4), suggesting an age spread smaller than our ±8 Myr. Literature estimates confirm this intuition. For example, Mamajek et al. (2002) find intrinsic 1σ age dispersions of 3 Myr in UCL. The relatively large uncertainty of the kinematic that we obtain may be artificially inflated by the fact that the component is composed of multiple clumps (Fig. 2) that,

---

[3]https://www.pas.rochester.edu/~emamajek/EEM_dwarf_UBVIJHK_colors_Teff.txt, version 2021.03.02

given a larger and more complete sample of kinematic data, would result in this component being subdivided further.

5.1.2 Age of USCO: component C

In contrast to the well constrained isochronal age of the Upper Centaurus-Lupus, literature estimates for the Upper Scorpius vary from 4 to 5 Myr for low-mass stars (Preibisch et al. 2002) to 11–13 Myr for intermediate-mass stars (Fang, Herczeg & Rizzuto 2017; Pecaut et al. 2012). Similar age discrepancies have been found by Rizzuto et al. (2016). Feiden (2016) and David et al. (2019) found that these discrepancies could be due to magnetic inhibition of convection and underestimated masses for low-mass stars, and argue that taking these effects into account produces an age estimate of 10 Myr for USCO, closer to the published value for intermediate stars than for low-mass stars. Sullivan & Kraus (2021) also argue that a population of undetected binary stars could be responsible for the inconsistent age estimates derived for low- versus intermediate-mass stars, and that correcting for this effect yields a consistent age of ∼10 Myr with a small intrinsic age spread (Sullivan & Kraus 2021). By contrast, Wright & Mamajek (2018) argue that USCO is an outcome of multiple bursts of star formation and thus has a real, substantial age spread. Similarly, Squicciarini et al. (2021) claim that star formation in USCO must have lasted more than 10 Myr.

Given that parts of component E overlap with component C, and some of the young stars in the USCO region are also members of component B, our model supports the view that Upper Scorpius is indeed a heterogeneous mixture of multiple populations with distinct kinematics and ages. Our kinematic age for component C is 4 ± 4 Myr, indicating an age spread comparable to the mean age. The large spread luminosity (about 2 magnitudes for M0 stars, a factor of a few larger than for component T; Fig. 3) supports the notion of multiple populations with different ages. More detailed kinematic analysis would be necessary to reliably disentangle the subcomponents and evaluate their individual ages.

5.1.3 Age of LCC: components A and U

The isochronal age for the LCC has also been controversial, but to a lesser extent. As Pecaut & Mamajek (2016) point out, the ages of UCL and LCC have typically been found to be very similar, i.e. 16 ± 1 Myr for UCL and 17 ± 1 Myr for LCC (Pecaut et al. 2012). Mamajek et al. (2002), however, find that LCC might be slightly younger than UCL, depending on the member selection. Moreover, de Geus et al. (1989) argue that UCL is slightly older, 14–15 Myr, while LCC is slightly younger, 11–12 Myr.

LCC in our kinematic model is split into two parts: component A in the upper and component U in the lower section. The kinematic age of the component A is 7 ± 5 Myr, while that of component U is 9 ± 4 Myr. While component A overlaps with the component T in the CMD, component U does not: it appears to be more overluminous than component A, and also has higher lithium content (Fig. 6). This confirms a report from Preibisch & Mamajek (2008) who state that 'there is some hint of substructure in the group, and it appears that the northern part of the group is somewhat more distant, older, and richer (∼17 Myr, 120 pc) than the southern part of the group (∼12 Myr, 110 pc).' Similarly, the work of Goldman et al. (2018) with ages based on the CIFIST evolutionary models (Baraffe et al. 2015) concludes that their groups A0 and A (lower LCC) are somewhat younger, age ∼7 Myr, than their groups B and C (upper LCC), with an age of 9–10 Myr. Likewise, Kerr et al. (2021) report on age gradient in the

LCC region decreasing from the north to the south. However, their northernmost part is older (23 ± 2.3 Myr) than our estimate, but the age of their component at $b = -10$ deg (13 ± 1.4 Myr) that falls within our component U agrees with our kinematic age.

5.1.4 Age of PDS 70

One of the members of component T is the T Tauri K star PDS 70, which hosts the protoplanet PDS 70b within a gap in its transition disk (Keppler et al. 2018; Müller et al. 2018). This is the first planet conclusively imaged during formation. Haffert et al. (2019) found a second protoplanet, PDS 70c, in the system, and Benisty et al. (2021) recently discovered a dust-depleted cavity in a circumplanetary disk around this planet.

Several surveys have measured the radial velocity of this star. *Gaia* DR2 (Sartoretti et al. 2018; Gaia Collaboration 2018) reports 3.1 ± 1.4 km s^{-1}, while Thanathibodee et al. (2020) and Žerjal et al. (2021) measure 6.0 ± 1.5 km s^{-1} and 5.1 ± 1.5 km s^{-1}, respectively. Using the *Gaia* radial velocity, as we do in our default analysis since this is the value with the smallest reported uncertainty, yields a 95 per cent membership probability in component T for this star. However, this does not change substantially if we use Žerjal et al.'s value of 5.1 ± 1.5 km s^{-1} instead: the membership probability in this case is 90 per cent. The location of the star in association is shown in Fig. 2.

Müller et al. (2018) estimate the age of PDS 70 to be 5.4 ± 1.0 Myr based on non-magnetic MIST models (Choi et al. 2016) coupled with a prior probability distribution that is flat in age and follows a Chabrier (2003) initial mass function in mass. This was already a very young age, largely inconsistent with the >10 Myr consensus age for stars in Upper Centaurus Lupus (Pecaut et al. 2012). Our kinematic age for component T is 15 ± 3 Myr, which is in even greater tension with Müller et al.'s age. Fig. 3 shows a narrow sequence of stars in the component, and constrains the age spread of stellar siblings to a small value. Comparison of the colour–magnitude diagram location of PDS 70 with that of component C also indicates that PDS 70 is likely older than Upper Scorpius. Finally, PDS 70's equivalent width of lithium (0.52 ± 0.07 Å, Žerjal et al. 2021) places it in between the 8 and 10 Myr lithium isochrones. We therefore conclude that PDS 70 is likely substantially older than Müller et al.'s estimate.

5.1.5 Age of TOI 1227

The southernmost part of the Lower Centaurus Crux (Fig. 2) is home to an M5 dwarf star TOI 1227 that hosts a sub-Jovian young planet with an estimated mass of $0.5 M_J$ and a radius of 0.85 ± 0.05 R$_J$ (9.5 R$_\oplus$; Mann et al. 2022). The authors suggest that young planet TOI 1227 b is still contracting and will evolve to an object with a radius smaller than 5 R$_\oplus$. They use lithium, stellar rotation, and the colour–magnitude diagram to derive an age of 11 ± 2 Myr. Our analysis assigns TOI 1227 to component U with ≈ 100 per cent membership probability, and Mann et al.'s age estimate is consistent with our kinematic age for component U (9 ± 4 Myr). We do not have radial velocity for this object in our database, but if we recompute the membership probability using the radial velocity of 13.3 ± 0.3 km s^{-1} reported by Mann et al., we reaffirm its membership.

5.2 On the purity and completeness of our membership list

The contamination of our membership list with old field stars is small, and thus the purity of our sample is very high. The contamination
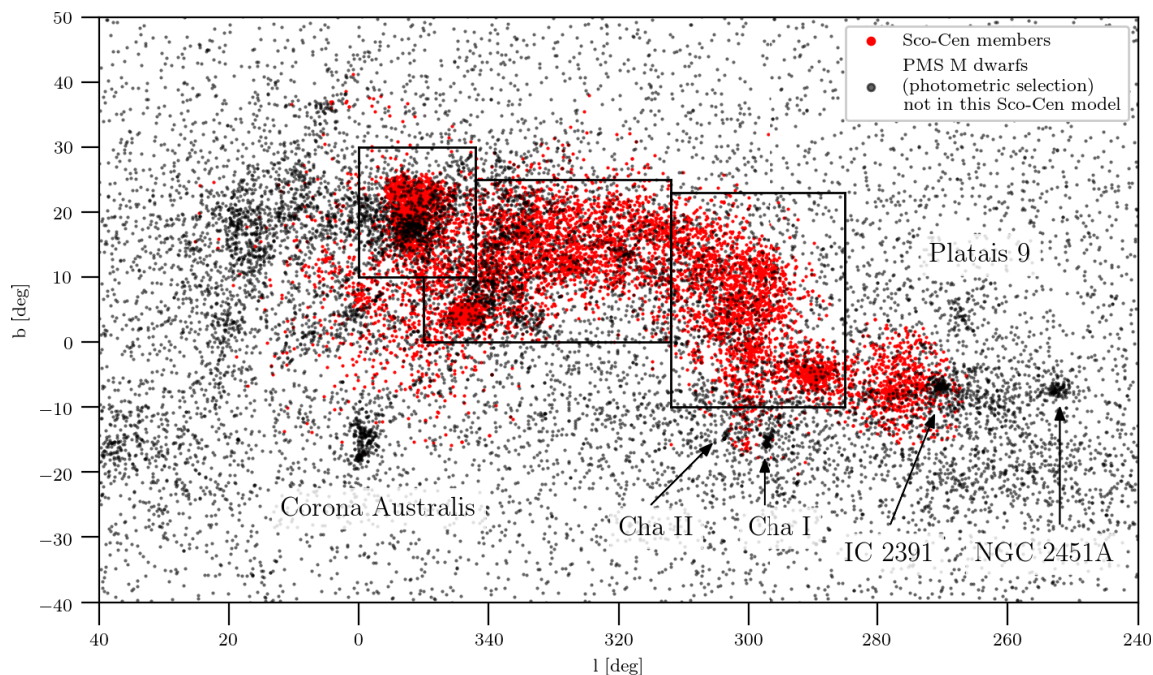
Figure 11. Sky positions of Sco–Cen members or potential members. Red points indicate stars kinematically identified as belonging to Sco–Cen in this work, while black points show pre-main sequence *M* dwarfs at distances of 80–200 pc, selected following Žerjal et al. (2021), that are *not* included in our CHRONOSTAR-based membership list. The PMS M dwarfs show additional substructure both within (e.g. in USCO) and around Sco–Cen that is not captured by our kinematic analysis. ⟲ .

rate is the highest in the low-mass region due to the missing radial velocities for M dwarfs and lower quality of astrometric measurements due to their intrinsically low luminosity. We thus estimate the contamination rate for M dwarfs with a membership probability of 90 per cent or better and Bp–Rp between 1.84 and 2.94 that corresponds to the M0 and M4 range. We count the number of these stars below and above the 20 Myr BHAC15 isochrone and provide the ratio between the two as a proxy for contamination. Using this method, we find that the contamination rate for components A, C, D, G, T, and U is below 5 per cent. However, approximately 15 per cent of M dwarfs in components E and F are likely contaminants. The reason for such high rates in component E is likely its complexity (see Section 4.4). Component F, on the other hand, was fitted with only 16 stars (Table 1) and is likely poorly constrained.

A small number of Sco–Cen members show depleted lithium (e.g. Figs 3 and 6). The membership probability of these objects is >90 per cent and they are clearly positioned on the young sequence of the colour–magnitude diagram. The source of the lithium measurements for the majority of the stars in the sample is from one of our previous papers (Žerjal et al. 2021) where the analysis was done automatically on a large number of spectra. We checked the allegedly lithium-depleted spectra and discovered lithium in them. The fact that all members of the association contain detectable lithium ensures low contamination rates.

However, our membership list is only partly complete: our model for Sco–Cen, meaning the eight well-defined components we identify, contains a total of 8185 stars with membership probability greater than 0.5 (4511 stars with 90 per cent membership probability). By contrast, the expected population of Sco–Cen is larger. Rizzuto et al. (2011) estimate that it contains 10 000 members, while Damiani et al. (2019) report nearly 11 000 pre-main-sequence stars with less than 3 per cent field-star contamination and ~3600 main-sequence candidate members with a larger (10–30 per cent) field-star

contamination rate. Out of 8185 members indentified from our work, 6990 objects are in common with Damiani et al. (2019): 1584 stars in G, 1290 in C, 1146 in A, 967 in T, 932 in E, 461 in D, 378 in U and 232 in component F.

The reason for the lower numbers in our model is our input catalogue defined by our selection boxes on the sky, which may not be large enough to include all Sco–Cen members. Our analysis may also assign some Sco–Cen members to the complex, poorly defined components B, J, and Q.

To understand these effects, we prepare an alternative list of young star candidates using photometric and distance selection; this will yield much lower purity than our kinematic catalogue, but higher completeness, allowing us to identify places where our kinematic catalogue misses potential members. For this purpose, we follow the selection criteria from Žerjal et al. (2021) who found that in the sample of M dwarfs with $B_P - R_P > 1.8$, ruwe <1.4 and M_G more than 1 mag above the main sequence, 80 per cent of them show spectroscopic signs of youth, e.g. lithium detection. With this selection we find 15 000 candidate young stars between 80 and 200 pc that are not members of our kinematic model but show overdensities within and around the traditional Sco–Cen boundaries in the sky; we show these stars, and our kinematically selected Sco–Cen members for comparison, in Fig. 11. We see that the most notable overdensities in our broader selection overlap with known clusters and associations, such as Corona Australis, Chamaeleon I and II, IC 2391 and NGC 2451A. The first three are known to be part of the Sco–Cen association but are not in our kinematic model either because they belong to the big complex components J, B, or Q (e.g. Corona Australis, Fig. 9) or because they were not in the input catalogue to the fit (e.g. IC 2391). It is clear that a more careful preparation of an initial catalogue would result in a better model describing all significant parts of an association that would yield a higher completeness ratio of the membership list.

6 CONCLUSIONS AND FUTURE WORK

We use CHRONOSTAR (Crundall et al. 2019) – a robust Bayesian method for kinematic age determination of young stellar associations – and *Gaia* DR2 data to construct a 6D kinematic model of the Sco–Cen association. Membership selection relies purely on the kinematics and completely neglects stellar age, location in the colour–magnitude diagram, or any other youth indicators. The main conclusions of this work are as follows:

(1) The Sco–Cen model identifies eight kinematically distinct components comprising more than 8000 stars distributed in dense and diffuse groups. Upper Centaurus-Lupus and LCC are split into two parts.

(2) Each of the components has an independently-fit kinematic age that is consistent with the isochronal age for K dwarfs, admittedly partly due to large uncertainties due to expected spreads in individual star ages. This is the first time the kinematic age in a complex association is determined reliably. The kinematic age of the two Upper Cantaurus-Lupus components is 15 ± 3 Myr and 13 ± 8 Myr. LCC, with ages of 7 ± 5 Myr and 9 ± 4 Myr for its two components, appears to be kinematically younger.

(3) We find that exoplanet host star PDS 70 has a 97 per cent membership probability in component T of Upper Centaurus-Lupus. The kinematic age of this component is 15 ± 3 Myr; this narrow age range is supported by a small luminosity spread for the stars that make up this component.

We conclude by noting that, while in this paper we have focused on Sco–Cen, there are obvious opportunities to our methods to other complex associations, which we intend to pursue in the future. Our analysis using CHRONOSTAR represents the first kinematic ages of the Sco–Cen association components that reliably agree with age estimates from other techniques. However, our method has the great advantage that it does not rely on predefined, uncertain membership lists, and, as we demonstrate here, can be run blind or semi-blind to discover structures and assign ages to them. It is fundamentally scalable, in a way that isochronal or lithium depletion ages are not. Application of our method will give us access to a map of how star formation occurs in space and time with unprecedented detail. Current work in our group is additionally exploring non-spherical component models and the addition of isochronal ages to improve membership probabilities and enable finer substructure to be obtained.

Software: CHRONOSTAR (Crundall et al. 2019), GALPY (Bovy 2015), DUSTMAPS (Green 2018), ASTROPY (Price-Whelan et al. 2018), NUMPY (Harris et al. 2020), IPYTHON (Pérez & Granger 2007), and MATPLOTLIB (Hunter 2007).

This work has made use of data from the European Space Agency (ESA) mission *Gaia* (https://www.cosmos.esa.int/gaia), processed by the *Gaia* Data Processing and Analysis Consortium (DPAC, https://www.cosmos.esa.int/web/gaia/dpac/consortium). Funding for the DPAC has been provided by national institutions, in particular the institutions participating in the *Gaia* Multilateral Agreement.

DATA AVAILABILITY

Results from this work are provided in Tables 1, 2, and C1. Full Tables 1 and C1 are available online as Supplementary Material. *Gaia* data (Gaia Collaboration 2018) is available on https://gea.esac.esa.int/archive/. Radial velocity measurements are taken from the GALAH DR3 survey (Buder et al. 2021), RAVE DR6 list (Steinmetz et al. 2020), APOGEE DR16 list (Ahumada et al. 2020), Žerjal et al. (2021), and a compiled table in the Banyan Σ paper (Gagné et al. 2018) – all references from their table are listed below Table C1. Equivalent widths of lithium are taken from Wheeler, Hogg & Ness (2021), Rizzuto et al. (2015), and Žerjal et al. (2019, 2021). We used evolutionary models computed by Baraffe et al. (2015) for *Gaia* filters G, B_P, and R_P and available on http://perso.ens-lyon.fr/isabelle.baraffe/BHAC15dir/BHAC15_iso.GAIA. Magnetic models from Feiden (2016) are found on https://github.com/gfeiden/MagneticUpperSco/. Empirical relations from 'A Modern Mean Dwarf Stellar Color and Effective Temperature Sequence' (Pecaut & Mamajek 2013) are found on https://www.pas.rochester.edu/~emamajek/EEM_dwarf_UBVIJHK_colors_Teff.txt.

REFERENCES

Ahumada R. et al., 2020, ApJS, 249, 3
Baraffe I., Homeier D., Allard F., Chabrier G., 2015, A&A, 577, A42
Benisty M. et al., 2021, ApJ, 916, L2
Binks A. S. et al., 2022, MNRAS, 513, 5727
Bobylev V. V., Baykova A. T., 2020, Astron. Rep., 64, 326
Bovy J., 2015, ApJS, 216, 29
Bovy J., 2017, MNRAS, 468, L63
Buder S. et al., 2021, MNRAS, 506, 150
Casagrande L. et al., 2021, MNRAS, 507, 2684
Chabrier G., 2003, PASP, 115, 763
Chen C. H., Mamajek E. E., Bitner M. A., Pecaut M., Su K. Y. L., Weinberger A. J., 2011, ApJ, 738, 122
Choi J., Dotter A., Conroy C., Cantiello M., Paxton B., Johnson B. D., 2016, ApJ, 823, 102
Covino E., Alcala J. M., Allain S., Bouvier J., Terranegra L., Krautter J., 1997, A&A, 328, 187
Crundall T. D., Ireland M. J., Krumholz M. R., Federrath C., Žerjal M., Hansen J. T., 2019, MNRAS, 489, 3625 (Paper I)
Dahm S. E., Slesnick C. L., White R. J., 2012, ApJ, 745, 56
Damiani F., Prisinzano L., Pillitteri I., Micela G., Sciortino S., 2019, A&A, 623, A112
David T. J., Hillenbrand L. A., Gillen E., Cody A. M., Howell S. B., Isaacson H. T., Livingston J. H., 2019, ApJ, 872, 161
de Geus E. J., de Zeeuw P. T., Lub J., 1989, A&A, 216, 44
de Zeeuw P. T., Hoogerwerf R., de Bruijne J. H. J., Brown A. G. A., Blaauw A., 1999, AJ, 117, 354
Dobbie P. D., Lodieu N., Sharp R. G., 2010, MNRAS, 409, 1002
Evans D. S., 1967, in Batten A. H., Heard J. F., eds, Proc. IAU Symp. 30, Determination of Radial Velocities and their Applications, Academic Press, London, p. 57
Fang Q., Herczeg G. J., Rizzuto A., 2017, ApJ, 842, 123
Feiden G. A., 2016, A&A, 593, A99
Gagné J. et al., 2018, ApJ, 856, 23
Gaia Collaboration, 2016a, A&A, 595, A1
Gaia Collaboration, 2016b, A&A, 595, A2

Gaia Collaboration, 2018, A&A, 616, A1

Gaia Collaboration, 2021, A&A, 649, A1

Galli P. A. B., Bouy H., Olivares J., Miret-Roig N., Sarro L. M., Barrado D., Berihuete A., Brandner W., 2020, A&A, 634, A98

Galli P. A. B. et al., 2021, A&A, 646, A46

Garcia B., Hernandez C., Malaroda S., Morrell N., Levato H., 1988, Ap&SS, 148, 163

Goldman B., Röser S., Schilbach E., Moór A. C., Henning T., 2018, ApJ, 868, 32

Gontcharov G. A., 2006, Astron. Lett., 32, 759

González M. et al., 2021, A&A, 647, A14

Green G. M., 2018, J. Open Source Softw., 3, 695

Guenther E. W., Esposito M., Mundt R., Covino E., Alcalá J. M., Cusano F., Stecklum B., 2007, A&A, 467, 1147

Gully-Santiago M. A. et al., 2017, ApJ, 836, 200

Haffert S. Y., Bohn A. J., de Boer J., Snellen I. A. G., Brinchmann J., Girard J. H., Keller C. U., Bacon R., 2019, Nature Astron., 3, 749

Hara A., Tachihara K., Mizuno A., Onishi T., Kawamura A., Obayashi A., Fukui Y., 1999, PASJ, 51, 895

Harris C. R. et al., 2020, Nature, 585, 357

Hunter J. D., 2007, Comput. Sci. Eng., 9, 90

Jeffries R. D. et al., 2017, MNRAS, 464, 1456

Johnson D. R. H., Soderblom D. R., 1987, AJ, 93, 864

Keppler M. et al., 2018, A&A, 617, A44

Kerr R. M. P., Rizzuto A. C., Kraus A. L., Offner S. S. R., 2021, ApJ, 917, 23

Kharchenko N. V., Scholz R. D., Piskunov A. E., Röser S., Schilbach E., 2007, Astron. Nachr., 328, 889

Kounkel M., Covey K., 2019, AJ, 158, 122

Kraus A. L., Hillenbrand L. A., 2008, ApJ, 686, L111

Kraus A. L., Cody A. M., Covey K. R., Rizzuto A. C., Mann A. W., Ireland M. J., 2015, ApJ, 807, 3

Krumholz M. R., McKee C. F., Bland-Hawthorn J., 2019, ARA&A, 57, 227

Leike R. H., Glatzle M., Enßlin T. A., 2020, A&A, 639, A138

Lopez Martí B., Jimenez Esteban F., Bayo A., Barrado D., Solano E., Rodrigo C., 2013, A&A, 551, A46

Luhman K. L., Esplin T. L., 2020, AJ, 160, 44

Makarov V. V., Olling R. P., Teuben P. J., 2004, MNRAS, 352, 1199

Mamajek E. E., Bell C. P. M., 2014, MNRAS, 445, 2169

Mamajek E. E., Meyer M. R., Liebert J., 2002, AJ, 124, 1670

Mann A. W. et al., 2022, AJ, 163, 156

Mermilliod J. C., Mayor M., Udry S., 2009, A&A, 498, 949

Miret-Roig N. et al., 2020, A&A, 642, A179

Müller A. et al., 2018, A&A, 617, L2

Murphy S. J., Lawson W. A., Bessell M. S., 2013, MNRAS, 435, 1325

Nelder J. A., Mead R., 1965, Computer J., 7, 308

Neuhäuser R. et al., 2000, A&AS, 146, 323

Pecaut M. J., Mamajek E. E., 2013, ApJS, 208, 9

Pecaut M. J., Mamajek E. E., 2016, MNRAS, 461, 794

Pecaut M. J., Mamajek E. E., Bubar E. J., 2012, ApJ, 746, 154

Pérez F., Granger B. E., 2007, Comput. Sci. Eng., 9, 21

Platais I., Kozhurina-Platais V., van Leeuwen F., 1998, AJ, 116, 2423

Prato L., 2007, ApJ, 657, 338

Preibisch T., Mamajek E., 2008, Nearest OB Association: Scorpius-Centaurus (Sco OB2). Astronomical Society of the Pacific, San Francisco, CA, p. 235

Preibisch T., Brown A. G. A., Bridges T., Guenther E., Zinnecker H., 2002, AJ, 124, 404

Price-Whelan A. M. et al., 2018, AJ, 156, 123

Rains A. D. et al., 2021, MNRAS, 504, 5788

Riedel A. R., Blunt S. C., Lambrides E. L., Rice E. L., Cruz K. L., Faherty J. K., 2017, AJ, 153, 95

Rizzuto A. C., Ireland M. J., Robertson J. G., 2011, MNRAS, 416, 3108

Rizzuto A. C., Ireland M. J., Kraus A. L., 2015, MNRAS, 448, 2737

Rizzuto A. C., Ireland M. J., Dupuy T. J., Kraus A. L., 2016, ApJ, 817, 164

Rizzuto A. C., Dupuy T. J., Ireland M. J., Kraus A. L., 2020, ApJ, 889, 175

Röser S., Schilbach E., Goldman B., Henning T., Moor A., Derekas A., 2018, A&A, 614, A81

Sartoretti P. et al., 2018, A&A, 616, A6

Schönrich R., Binney J., Dehnen W., 2010, MNRAS, 403, 1829

Schutz K., Lin T., Safdi B. R., Wu C.-L., 2018, Phys. Rev. Lett., 121, 081101

Siebert A. et al., 2011, AJ, 141, 187

Somers G., Pinsonneault M. H., 2015, ApJ, 807, 174

Squicciarini V., Gratton R., Bonavita M., Mesa D., 2021, MNRAS, 507, 1381

Steinmetz M. et al., 2020, AJ, 160, 82

Sullivan K., Kraus A. L., 2021, ApJ, 912, 137

Thanathibodee T. et al., 2020, ApJ, 892, 81

Torres C. A. O., Quast G. R., da Silva L., de La Reza R., Melo C. H. F., Sterzik M., 2006, A&A, 460, 695

Wheeler A. J., Hogg D. W., Ness M., 2021, ApJ, 908, 247

White R. J., Gabor J. M., Hillenbrand L. A., 2007, AJ, 133, 2524

Wilson R. E., 1953, General Catalogue of Stellar Radial Velocities, Carnegie Institute Washington D.C. Publication

Wright N. J., Mamajek E. E., 2018, MNRAS, 476, 381

Yen S. X., Reffert S., Schilbach E., Röser S., Kharchenko N. V., Piskunov A. E., 2018, A&A, 615, A12

Žerjal M. et al., 2019, MNRAS, 484, 4591

Žerjal M. et al., 2021, MNRAS, 503, 938

SUPPORTING INFORMATION

Supplementary data are available at *MNRAS* online.

Table 1. Components in the Sco–Cen model today (time t) and at birth (time 0).

Table C1. List of stars that have membership probabilities at least 50 per cent in any of the components in the Scorpius-Centaurus association. Column `comp` denotes the component the star belongs to with the membership probability p.

Please note: Oxford University Press is not responsible for the content or functionality of any supporting materials supplied by the authors. Any queries (other than missing material) should be directed to the corresponding author for the article.

APPENDIX A: EPICYCLIC APPROXIMATION

Numerical integration of Galactic orbits is replaced by a computationally efficient epicyclic approximation in the curvilinear coordinate system following Makarov, Olling & Teuben (2004). The origin of this non-inertial coordinate system is set in the LSR at the Galactocentric radius R_{LSR} that rotates around the Galactic centre at a constant rate. The radial component ξ points towards the Galactic centre at all times. The tangential component η is positive in the direction of the Galactic rotation and ζ is displacement from the Galactic plane. The position of a star (ξ, η, ζ) at a given time t close to the LSR is approximated with

$$\xi(t) = \xi_0 + \dot{\xi}_0 \kappa^{-1} \sin \kappa t + (\dot{\eta}_0 - 2A\xi_0)(1 - \cos \kappa t)(2B)^{-1}$$

$$\begin{aligned}\eta(t) = \eta_0 &- \dot{\xi}_0 (1 - \cos \kappa t)(2B)^{-1} \\ &+ \dot{\eta}_0 (A\kappa t - (A - B)\sin \kappa t)(\kappa B)^{-1} \\ &- \xi_0 2A(A - B)(\kappa t - \sin \kappa t)(\kappa B)^{-1}\end{aligned}$$

$$\zeta(t) = \zeta_0 \cos \nu t + \dot{\zeta}_0 \nu^{-1} \sin \nu t. \tag{A1}$$

Velocities are determined by the first derivatives of the position:

$$\dot{\xi}(t) = \dot{\xi}_0 \cos \kappa t + (\dot{\eta}_0 - 2A\xi_0)\kappa \sin \kappa t (2B)^{-1}$$

$$\begin{aligned}\dot{\eta}(t) = &-\dot{\xi}_0 \kappa (2B)^{-1} \sin \kappa t + \dot{\eta}_0 B^{-1}(A - (A - B)\cos \kappa t) \\ &- 2A\xi_0 (A - B)(1 - \cos \kappa t)B^{-1}\end{aligned}$$

$$\dot{\zeta}(t) = -\zeta_0 \nu \sin \nu t + \dot{\zeta}_0 \cos \nu t. \tag{A2}$$

The initial positions (ξ_0, η_0, ζ_0) and $(\dot{\xi}_0, \dot{\eta}_0, \dot{\zeta}_0)$ are free parameters of the fit. In practice, CHRONOSTAR operates in the Cartesian space.
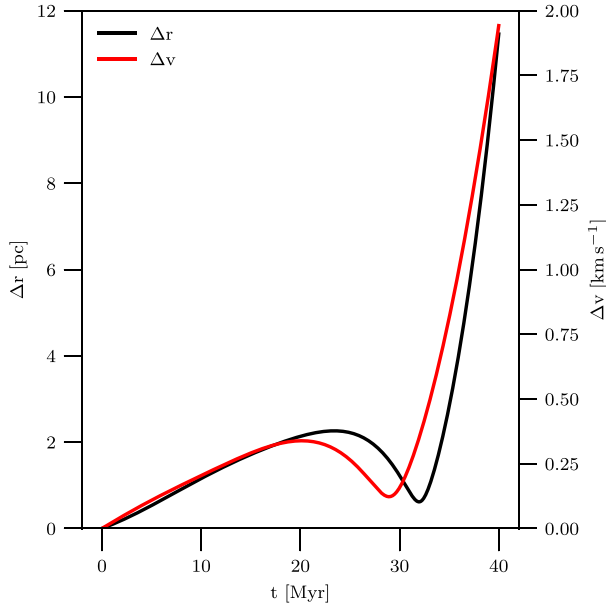
Figure A1. Epicyclic orbit approximates numerically integrated GALPY trajectory within $\Delta r = 2$ pc and $\Delta v = 0.3$ km s^{-1} for $\sim$30 Myr. Δr and Δv are absolute differences between GALPY and epicyclic orbits. ◯ .

The conversion between the Cartesian and curvilinear systems is in place solely for the epicyclic approximation.

Epicyclic frequencies κ and ν are related to the Oort's constants $A = 15.3 \pm 0.4$ km s^{-1} kpc^{-1} and $B = -11.9 \pm 0.4$ km s^{-1} kpc^{-1} (Bovy 2017) by

$$\kappa = \sqrt{-4B(A - B)},$$
$$\nu = \sqrt{4\pi G\rho + (A + B)(A - B)}, \qquad (A3)$$

where $\rho = 0.0889 \pm 0.0071$ M$_\odot$ pc^{-3} (Schutz et al. 2018).

Since these values were determined from a much bigger volume of data, i.e. Oort's constants at a typical heliocentric distance of 230 pc, and the density at the kiloparsec scale, we fine tuned constants A, B, and ρ to match the GALPY orbits at the Sco–Cen distance more precisely:

$$A' = 0.89\,A, \; B' = 1.15\,B, \; \rho' = 1.21\,\rho. \qquad (A4)$$

This gives $\kappa = 0.04$ Myr^{-1} and $\nu = 0.08$ Myr^{-1}. Such epicyclic approximation for a star in USCO is valid for $\sim$30 Myr when the difference with galpy orbit integration starts to increase significantly over time, i.e. beyond 2 pc and 0.3 km s^{-1} (Fig. A1).

Table B1. Median extinction A_G and standard deviation σ_{A_G} in *Gaia* DR2 *G* for members with >50 per cent membership probability and $0.2 < (B_P - R_P)_0 < 2$. Components C, D, and F are affected by relatively high extinction. ◯ .

ID	Median A_G mag	σ_{A_G} mag
A	0.10	0.03
C	0.62	0.42
D	0.51	0.21
E	0.21	0.43
F	0.41	0.31
G	0.11	0.07
H	0.16	0.05
I	0.08	0.02
T	0.11	0.03
U	0.14	0.05

APPENDIX B: REDDENING CORRECTION

Sco–Cen is located in the Galactic plane rich in dust. This means that the measured *Gaia* magnitudes in our catalogue are affected by interstellar extinction. To correct for reddening, we use the procedure from Rains et al. (2021)[4] that uses the 3D dust map of Leike, Glatzle & Enßlin (2020) and is implemented in the python package dustmaps (Green 2018). Extinction coefficients for *Gaia* DR2 *G*, B_P and R_P bands were determined from the $B_P - R_P$-dependent relation found in Casagrande et al. (2021). We apply this relation on the entire sample but note that it is only valid for $0.2 < (B_P - R_P)_0 < 2$. Median values of extinction and associated standard deviations are determined for each component with stars having >50 per cent membership probability and presented in Table B1. Apart from the complex component E, the largest spread in extinction is seen in components C and F – the former can be explained by a spatial substructure within the component covering multiple regions. The median extinction for the majority of the Sco–Cen components is low. The estimates are based on stars with $0.2 < (B_P - R_P)_0 < 2$. Since stars redder than $(B_P - R_P)_0 = 2$ are located in the same interstellar environment we assume that they are affected by a similarly low reddening.

APPENDIX C: MEMBERSHIP PROBABILITIES

[4]https://github.com/adrains/plumage

Table C1. List of stars that have membership probabilities at least 50 per cent in any of the components in the Scorpius–Centaurus association. Column COMP denotes the component the star belongs to with the membership probability p. (BP-RP)$_0$ and G$_0$ are corrected for extinction. Reference column reports on the source for radial velocity/lithium. References: (1) Žerjal et al. (2019), (2) Gaia Collaboration et al. (2018), (3) Covino et al. (1997), (4) Mermilliod, Mayor & Udry (2009), (5) Lopez Martí et al. (2013), (6) Prato (2007), (7) White, Gabor & Hillenbrand (2007), (8) Siebert et al. (2011), (9) E. Bubar et al. 2018 in preparation, (10) Gontcharov (2006), (11) Steinmetz et al. (2020), (12) Chen et al. (2011), (13) Torres et al. (2006), (14) Žerjal et al. (2021), (15) Wilson (1953), (16) Guenther et al. (2007), (17) Dahm, Slesnick & White (2012), (18) Murphy et al. (2013), (19) Ahumada et al. (2020), (20) Garcia et al. (1988), (21) Buder et al. (2021), (22) Rizzuto et al. (2015), (23) Kharchenko et al. (2007), (24) Evans (1967). Full table is available online as Supplementary Material.

Source_id Gaia DR2	(BP-RP)$_0$	G$_0$	RV (km s⁻¹)	σ_{RV} (km s⁻¹)	X (pc)	Y (pc)	Z (pc)	U (km s⁻¹)	V (km s⁻¹)	W (km s⁻¹)	σ_X (pc)	σ_Y (pc)	σ_Z (pc)	σ_U (km s⁻¹)	σ_V (km s⁻¹)	σ_W (km s⁻¹)	Comp	p	EW(Li) Å	$\sigma_{EW(Li)}$ Å	Ref RV/Li
6110141563309613056	1.63	11.49	3.1	1.4	79.7	−71.6	62.3	2.3	−5.6	1.4	0.4	0.3	0.2	1.0	0.9	0.5	T	0.95	0.52	0.07	2/14
6074563978391541504	2.15	12.89	12.4	1.2	59.1	−99.1	42.5	1.8	−9.1	0.9	0.4	0.7	0.1	0.6	1.1	0.2	A	0.98	0.36	0.07	2/14
6075267425304250880	1.96	13.23	8.3	5.8	83.7	−125.8	54.3	1.7	−5.7	0.6	0.4	0.5	0.1	3.2	4.8	1.1	T	0.59	0.20	0.01	2/1
5969266120643392256	1.21	11.42	1.8	1.1	170.9	−53.8	38.9	6.9	−8.1	3.8	2.2	0.7	0.2	1.1	0.4	0.2	D	1.00	0.13	0.07	2/14
6017469427618958208	0.93	10.79	2.9	1.2	169.7	−52.3	42.5	8.4	−7.6	3.2	1.5	0.5	0.2	1.1	0.4	0.3	D	0.93	0.40	0.07	2/14
6106733691438736128	1.65	12.18	4.8	0.8	103.9	−72.7	75.7	6.2	−7.3	2.1	0.7	0.1	0.4	0.6	0.4	0.3	T	0.99	0.48	0.07	2/14
6249055271112519936	1.37	11.17	−4.4	7.4	134.3	−13.3	86.8	7.8	−2.9	0.6	1.3	0.1	0.6	6.7	0.7	3.1	C	1.00	0.47	0.02	2/22
6051498079848359296	2.11	11.95	−14.4	5.3	140.5	−9.2	68.9	−2.0	0.0	−1.9	1.7	0.1	0.5	5.1	0.4	1.6	C	0.97	0.73	0.02	2/22
6235172592479759232	1.63	11.80	−3.1	6.9	130.2	−34.5	82.2	5.5	−6.1	1.0	1.1	0.3	0.2	6.1	1.6	2.7	T	0.83	0.48	0.02	2/1
6086395513764172416	2.15	13.04	10.1	3.8	70.2	−97.7	60.2	3.5	−8.2	1.5	0.5	0.6	0.3	2.1	3.0	1.1	G	0.63	0.30	0.02	2/1
6014331906769737984	2.03	12.61	−1.4	6.4	108.6	−46.3	62.9	3.4	−6.8	1.4	0.8	0.3	0.3	5.6	2.4	2.0	C	0.94	0.48	0.01	2/1
6244337679032642688	1.79	12.18	−8.0	1.6	131.4	−13.8	74.4	3.6	−2.0	0.2	0.8	0.1	0.3	1.5	0.2	0.6	C	1.00	0.60	0.02	2/22
6013772083535731968	1.63	11.79	4.9	7.4	120.4	−56.1	66.8	8.9	−7.7	3.0	1.3	0.6	0.4	6.4	3.0	2.2	G	0.50	0.31	0.02	2/1
6242626387962771456	1.81	12.10	−6.0	0.9	131.3	−18.4	74.3	5.8	−4.0	−1.7	1.1	0.1	0.4	0.8	0.2	0.3	C	1.00	0.52	0.01	2/1
6107169755177631872	1.67	12.58	2.6	4.3	94.4	−105.7	62.8	0.2	−3.8	−0.6	0.8	0.9	0.3	2.7	3.1	1.1	T	1.00	0.30	0.01	2/1
6093133488520130176	1.38	11.94	8.3	1.7	122.2	−107.3	63.7	5.4	−8.9	2.4	1.0	0.9	0.3	1.3	1.1	0.4	G	0.61	0.47	0.07	2/14
6099876213515229184	1.47	11.91	8.1	1.0	110.5	−87.1	64.0	7.2	−8.7	2.0	0.9	0.7	0.3	0.8	0.6	0.3	T	0.99	0.43	0.07	2/14
6038520956430662144	1.91	12.46	−2.7	2.1	124.0	−30.0	59.9	6.1	−4.6	0.4	0.6	0.1	0.2	2.0	0.5	0.6	E	0.96	0.55	0.03	2/22
6208713089974550656	1.95	13.04	−5.7	6.5	125.2	−47.3	75.1	0.8	−4.7	0.8	1.0	0.4	0.4	5.7	2.2	2.3	G	0.80	0.36	0.01	2/1
6050978698041931776	1.75	11.89	−8.1	9.9	131.2	−13.7	67.1	4.2	−2.6	−2.8	0.7	0.1	0.2	9.4	1.0	3.0	C	1.00	0.55	0.01	2/1
6039021371655978112	1.37	11.05	−7.5	3.4	150.6	−28.2	66.0	2.6	−3.1	−0.9	2.3	0.4	0.6	3.2	0.6	0.9	E	0.86	0.22	0.02	2/1
5215814919990121856	1.77	11.51	17.0	1.4	38.0	−98.2	−10.2	−1.0	−8.1	−2.9	0.4	1.1	0.4	0.5	1.3	0.5	U	0.71	0.48	0.07	2/14
6107185251419688320	1.87	12.73	6.5	6.0	88.3	−99.3	60.8	2.7	−6.6	0.7	0.7	0.8	0.3	3.8	4.3	1.6	T	1.00	0.42	0.00	2/1
6260746481328616448	1.83	12.52	−5.9	3.9	132.9	−15.2	93.9	6.1	−3.5	0.5	1.1	0.1	0.6	3.4	0.4	1.8	C	0.94	0.57	0.01	2/1
6135468641852927744	2.14	12.85	9.6	0.7	55.4	−84.0	58.0	2.4	−8.0	1.2	0.2	0.4	0.1	0.4	0.5	0.2	T	0.56	0.21	0.07	2/14
6102544590795328896	1.98	12.85	3.5	2.5	122.5	−100.2	70.1	2.1	−7.6	0.4	4.7	3.8	1.7	1.9	1.6	0.7	T	0.94	0.38	0.01	2/1
6049726075120913152	1.30	11.64	−4.1	1.5	146.9	−22.5	75.8	6.5	−4.1	0.6	1.0	0.2	0.2	1.4	0.2	0.5	C	0.90	0.35	0.07	2/14
6048935358761628288	1.84	11.90	−8.0	6.7	130.5	−17.7	63.3	3.4	−2.0	−1.9	0.7	0.1	0.2	6.4	0.9	1.9	C	0.99	0.52	0.02	2/22
6050388913137070848	1.86	12.62	−4.7	1.4	130.4	−18.1	71.7	6.9	−4.1	−1.4	0.9	0.1	0.3	1.3	0.2	0.5	C	1.00	0.43	0.01	2/1
6017410053991075584	1.14	11.41	0.9	1.1	165.4	−50.4	40.1	6.5	−7.4	3.1	1.4	0.4	0.1	1.0	0.4	0.1	D	1.00	0.54	0.07	2/14
6043809637411589376	1.39	11.59	−3.0	1.3	146.2	−26.7	78.0	7.0	−7.0	0.1	0.9	0.2	0.3	1.2	0.3	0.4	C	0.65	0.40	0.07	2/14
6240832435964142080	1.25	11.30	−3.2	0.5	125.7	−23.7	84.8	6.5	−5.1	2.4	0.7	0.1	0.3	0.5	0.1	0.2	E	0.54	0.39	0.07	2/14
6237148384817472256	1.74	12.28	−7.5	1.3	129.5	−24.8	79.4	2.9	−4.7	−0.6	0.8	0.2	0.3	1.2	0.3	0.5	C	1.00	0.41	0.01	2/1
6244019542218710912	1.52	11.31	−17.1	4.9	125.5	−16.4	78.6	−4.0	−2.4	−5.7	0.9	0.1	0.4	4.5	0.6	1.9	C	1.00	0.59	0.02	2/22
6127032325352993024	1.89	12.24	11.7	0.8	50.6	−96.0	50.8	1.8	−8.0	0.6	0.2	0.4	0.1	0.4	0.7	0.2	A	0.96	0.39	0.02	2/1

This paper has been typeset from a T$_{\rm E}$X/l$^{\!A}$T$_{\rm E}$X file prepared by the author.